Check for updates

ADVANCED ENERGY MATERIALS
www.advenergymat.de

Vanadium-Based Cathodes Modification via Defect Engineering: Strategies to Support the Leap from Lab to Commercialization of Aqueous Zinc-Ion Batteries

Xin Zeng, Zhe Gong, Cheng Wang, Patrick J. Cullen, and Zengxia Pei**

In advancing aqueous zinc-ion batteries (AZIBs) toward commercial viability, vanadium (V)-based cathodes are pivotal, offering broad redox ranges, and compatibility with water's electrochemical limits. Despite their great potentials, V-based cathodes face challenges in transitioning from lab to commercialization. Defect engineering is exploited as a pivotal technique that endows the cathodes with unexpected physical and chemical properties to break the intrinsic bottleneck and, in turn, enhance their electrochemical performances. This review delves into the role of defect engineering on V-based materials, underscoring its potential in mitigating the critical challenges. It starts by encapsulating the current characteristics of V-based cathodes in AZIBs. Research efforts related to various defects, such as oxygen vacancies, cation vacancies, cationic doping, anionic doping, water intercalation, and lattice disorders/amorphization, are then rationalized and discussed. The fabrication and characterization techniques of defect engineering are also summarized. By integrating the conclusions from existing works and tailoring defect engineering strategies, a few perspectives are provided for systematically employing defect engineering to pave the way for a more efficient transition of these promising materials from laboratory breakthroughs to commercially viable energy storage solutions.

1. Introduction

Renewable energy's greater integration into current electrical grids necessitates the development of large-scale, cost-effective energy storage technologies, such as rechargeable batteries.[1] Citing concerns about safety, cost, and sustainability, existing non-aqueous Li-ion battery (LIB) technology is not suited for large-scale applications.[2] In spite of the resource efficiency of other types of non-aqueous Na^+ and K^+ batteries for large-scale applications, their safety remains an ongoing concern due to the volatile organic electrolytes deployed.[3] To address safety and economic concerns, liquid electrolytes could be converted from organic to aqueous ones. This alternative has many advantages, including intrinsic safety, reduced costs, enhanced ionic conductivity, and simplified ambient manufacturing. Allured by these distinct advantages, several aqueous rechargeable batteries based on alkali metal cations (e.g., Na^+ and K^+) and multivalent cations (e.g., Mg^{2+}, Ca^{2+}, Zn^{2+}, and Al^{3+}) have been extensively scrutinized in the last few years.[4] Given the nature of multi-electron transfer, high volumetric capacity and energy density are naturally anticipated for multivalent cation chemistry over the monovalent counterparts. In this context, rechargeable AZIBs that are primarily constituted of a zinc (Zn) metal anode, a Zn salt-based aqueous electrolyte, and a host cathode, stand out as one of the most attractive candidates. Apart from the superior nature of safety and environmental benignity, the utilized Zn is cost-effective, sustainable, with mature technology for production and extraction. More critically, Zn anode has a high theoretical capacity (820 mAh g^{-1}, 5854 mAh cm^{-3}), a suitable redox potential (−0.76 V vs standard hydrogen electrode (SHE)), and relatively low polarizability (compared with other metal anodes like Mg and Al).[5] Actually, Zn has been advocated as the most viable metal electrode that is compatible with aqueous electrolytes and with satisfactory reaction kinetics (which is essential for rechargeability).[6] Based on these advantages, AZIBs are deemed one of the most promising post-LIB systems for sustainable large-scale energy storage.

Despite the prospects depicted from the Zn anode and the aqueous nature, developing high-performance cathodes that can fully leverage the above advantages for next-generation AZIBs is of vital significance. So far, promising cathode materials of AZIBs have been primarily found in V-based materials, manganese oxides, Prussian blue analogues, organic compounds, and others.[7] Many excellent reviews that compare the cons and pros of these cathode materials are available elsewhere.[8] In general, manganese oxides possess moderate voltage and satisfactory

X. Zeng, Z. Gong, C. Wang, P. J. Cullen, Z. Pei
School of Chemical and Biomolecular Engineering
The University of Sydney
Sydney, New South Wales 2006, Australia
E-mail: cwan5232@uni.sydney.edu.au; zengxia.pei@sydney.edu.au

The ORCID identification number(s) for the author(s) of this article can be found under https://doi.org/10.1002/aenm.202401704

© 2024 The Author(s). Advanced Energy Materials published by Wiley-VCH GmbH. This is an open access article under the terms of the Creative Commons Attribution-NonCommercial License, which permits use, distribution and reproduction in any medium, provided the original work is properly cited and is not used for commercial purposes.

DOI: 10.1002/aenm.202401704

theoretical capacity, but the unstable crystal structure and Mn^{2+} dissolution caused by the Jahn-Teller effect hasten their capacity degradation.[9] Although Prussian blue analogues have a stable crystal structure and relatively high voltage (≥1.5 V vs Zn), the associated poor capability (specific capacity below 100 mAh g^{-1}) has substantially hampered their future application.[10] The organic compounds are highly tunable but usually with sluggish reaction kinetics and complex electrochemical reaction mechanisms.[11] In contrast, V-based materials have a high theoretical capacity, greater rate performance, and longer cycle life, rendering them a better fit for high-performance AZIBs. Almost 40 years of research has been conducted on V-based materials as suitable cathode materials in various battery systems, due to the materials' unique features including wide range of oxidation states (V^{2+}, V^{3+}, V^{4+}, V^{5+}), distinct structures (layered, tunnel, NASICON type), miscellaneous coordination environments (tetrahedra, trigonal bipyramids, square pyramids, regular octahedra, distorted octahedra), and natural abundance.[12] While the long-term development and optimization of cathode materials in AZIBs aim to simultaneously achieve high specific capacity, high rate performance, and extended cycle life, these goals remain daunting challenges. Thus, the immediate focus for grid-level energy storage may lie in achieving long-term cyclic stability and durability. In this regard, V-based materials, already recognized for their relatively impressive cycle stability, undoubtedly hold considerable potential. Within this context, the most pressing challenge becomes addressing structural degradation and active material dissolution in aqueous systems, particularly under realistic conditions of low current and slow cycling. Overcoming these hurdles is essential for maximizing the effectiveness of V-based materials in large-scale energy storage, aligning them with the short-term priorities of the energy storage sector.

Defect engineering has been rationalized as an effective strategy to modulate electrode materials' electronic properties and enhance their electrochemical performances, offering promising solutions to the aforementioned challenges. Specifically, for V-based materials, defect engineering is effective in several critical aspects including (but not limited to) providing more active sites, accelerating ion diffusion, optimizing conductivity, and enhancing structural stability. In the last a few years, new strategies and technologies of the introduction and characterization of defects are being developed and/or exploited. Meanwhile, many mechanisms and/or the underlying roles of distinct defect sites (e.g., intercalated water) have been continuously unraveled. Consequently, the electrochemical performance of electrode materials can be greatly enhanced by defect engineering.

Herein, in this timely review, we aim to provide a systematic introduction of the recent progress on rational designing advanced V-based AZIBs cathode materials through defect engineering, as well as their internal relationship with Zn^{2+} ion transfer kinetics. We start with analyzing the gaps between research and practical application requirements, with key notorious problems of V-based cathode materials defined. With the summary of six defect types (i.e., oxygen vacancy, cation vacancy, cationic doping, anionic doping, water intercalation, and lattice disorder/amorphization), their specific impacts on V-based electrode materials for AZIBs are systematically rationalized and exemplified with pertinent recent advances. Subsequently, the strategies for the introduction of the defects are also summarized as per two predominant approaches: chemical and physical ones. Then, advanced technologies for defect characterizations along with the theoretical calculation methods are summarized. The last segment of our review provides insights into the future of defects engineering, with the intention of developing high-performance AZIBs.

2. From Mechanism Insight of Vanadium-Based Cathodes to Choosing the Suitable Tools for Practical Use

2.1. The Gap Between Research and Practical Application

In the context of AZIBs, V-based cathode materials, particularly vanadium oxides, stand out due to their extensive redox range which complements the potential window of water. Their large interlayer spacing typically enables high discharge capacities, epitomizing them as quintessential representatives in Zn^{2+} intercalation chemistry. However, these vanadium oxide materials in aqueous systems face challenges of structural degradation and active material dissolution, caused by repetitive electrochemical reactions with Zn^{2+} ions that possess a relatively large hydration radius. Recent advancements, employing the "pillar effect" strategy (introducing guest species such as cations or polymers into the interlayers of cathode materials), have significantly improved the stability of vanadium oxide materials.[13] Especially under high current cycling greater than 1 C, the pseudocapacitive behavior induced at the electrode material surface, in addition to diffusion processes, contributes to enhanced cycle stability.

Nevertheless, upon the low-current, slow cycling that is required in realistic energy storage scenarios, the structural instability and slow structural collapse of V-based cathode materials under would substantially limit their practical application and confine their cycle life. Although the fundamental cause of this phenomenon remains a matter of debate, two key factors are used ascribed to: 1) intensified V dissolution and associated interfacial by-products during deep cycling; 2) increased structural stress caused by the continual intercalation of Zn^{2+} ions into the host lattice. For AZIBs with V-based cathodes aimed at grid energy storage, exceedingly long cycle stability and low maintenance costs are of high demands. Hence, the optimal approach is to control and address these core issues at the material structure level.

Defect engineering, by introducing defects to modulate the electronic and structural features of cathode materials, is an effective strategy in addressing these core challenges. Crystallographic defects, such as vacancies, antisites, and dislocations, can regulate the physical and chemical properties of crystal materials, thus affecting the corresponding electrochemical performances.[14] For the former cause as listed above, defect engineering can enhance the structural stability of the cathode materials, suppressing the dissolution of active materials. In theory, a stable crystal structure is typically thermodynamically insoluble, suggesting that V-based cathode materials with more stable crystal structures may exhibit lower degrees of V dissolution. For the latter cause, defect engineering can effectively reduce the strong electrostatic interactions between the host and multivalent ions with large charges, mitigating changes in structural stress and improving ion transport kinetics.[15] Thus, defect engineering might

© 2024 The Author(s). Advanced Energy Materials published by Wiley-VCH GmbH

16146840, 2024, 31, Downloaded from https://advanced.onlinelibrary.wiley.com/doi/10.1002/aenm.202401704 by University of Adelaide Alumni, Wiley Online Library on [02/04/2025]. See the Terms and Conditions (https://onlinelibrary.wiley.com/terms-and-conditions) on Wiley Online Library for rules of use; OA articles are governed by the applicable Creative Commons License

be pivotal to realizing V-based cathode materials with stable crystal structures and their practical application.

Beyond addressing the two core issues, defect engineering, tailored to specific needs during the synthesis of electrode materials, endow them with novel functionalities. For instance, synergistic effects of defect engineering can activate the otherwise inert electrodes, yielding ion storage locations. Meanwhile, generating vacancies could lead to partial reduction of V, resulting in mixed-valence V materials with enhanced electrical conductivity due to charge compensation effects.[16] However, at this stage, achieving highly effective multifaceted effects through a single type of defect seems exceedingly challenging. Prioritizing the development of singular defects that address the two core issues appears more pragmatic, potentially accelerating the journey towards practical application. Alternatively, developing materials with multiple types of defects working in synergy for multifaceted effects is feasible, although this poses greater demands on defect control methods.

2.2. From Mechanisms to Practical Needs

The V-based compounds have multiple oxidation states that offer rich redox reactions as electrode materials.[17] A variety of V-based electrode materials have been scrutinized, which can mainly be divided into vanadium oxides, vanadates, vanadium phosphates, and oxygen-free V-based compounds.

The most widely studied V-based material is vanadium oxide, such as orthorhombic α-V_2O_5, monoclinic VO_2(B), bilayered $V_2O_5{\cdot}nH_2O$, and trigonal V_6O_{13}. In particular, V_2O_5, as one of the most common electrode materials, has a layer spacing much greater than that of Zn^{2+} ions.[18] In theory, it can provide a theoretical capacity up to 589 mAh g^{-1} based on the two-electron redox center ($V^{5+} \leftrightarrow V^{3+}$).[19] While the structure is unstable and faces the risk of collapsing under repeated insertions of a large number of Zn^{2+}, defect engineering has been used to optimize the cycle stability of the material, as discussed later. Another main type of most commonly used V-based electrode material is Vanadate. The ease with which V-O polyhedrons can be deformed and the wide range of valence states of V contribute to the structure's exceptional capability to form composite with other cations (like alkali metal ions, alkali earth metal ions, transition metal ions, NH_4^+), thereby generating many derivatives which are called vanadates. Depending on the types of cations introduced, the V valence state, and the A/V ratio (A is the introduced cation), the final vanadates have significant structural differences and distinct electrochemical properties. As for vanadium phosphate materials, the main characteristic is the presence of [PO_4] tetrahedrons within the structure, which gives them unique crystal structures and electrochemical properties. In most vanadium phosphates (such as $Li_3V_2(PO_4)_3$), corner-sharing connections are used to construct 3D open-framework structures by using octahedrons [VO_6] and tetrahedrons [PO_4], whereas few are layered.[20] Although vanadium phosphate has a stable structure and high ion diffusion coefficient, generally it has poor electronic conductivity because the [VO_6] octahedrons are separated by phosphate groups. Lastly, oxygen-free V-based compounds (e.g., vanadium chalcogenides, V-based MXenes) are also used as cathodes in AZIBs.[21] However, these materials are all too often unstable and will undergo phase changes when operated in aqueous electrolytes. The evolved structures behave more resembling the aforementioned (doped) vanadium oxides.

The diffusion pathways in various types of V-based cathode materials can be categorized based on their lattice structures, ranging from one to 3D diffusion channels. With the increase in dimensionality, the availability of pathways for Zn^{2+} ion diffusion increases, facilitating rapid Zn^{2+} ion storage.[22] Similarly, defects can be classified based on their dimensions into three types: point defects, linear defects, and planar defects. Therefore, the synergy between defect engineering and the dimensionality of diffusion channels can fulfill the structural design requirements of various V-based cathodes. By designing and constructing multidimensional defects, represented by point defects (such as vacancies, interstitial atoms, or substitutions) and/or linear and planar defects (represented by dislocations and boundary formations),[23] it's possible to enhance the electrochemical performance of electrode materials, particularly aiming for the objective of prolonged cycle stability.

The general key problems of V-based cathode materials are summarized as follows:

-**Low operating voltage (low energy density)**: The average operating voltage of V-based cathode materials in aqueous solution is only ≈0.8 V (**Figure 1a**). Oversight the influence of operating voltage leads to poor energy density diminishing the practical applicability of AZIBs. For instance, a cathode material with a specific capacity of 300 mAh g^{-1} operating at 0.6 V versus Zn/Zn^{2+} combined with a Zn anode utilized at 50% (a realistic scenario), would yield a Zn-ion cell with a specific energy below 100 Wh kg^{-1}. Conversely, a cathode material with a lower capacity of 100 mAh g^{-1} but operating at a higher potential of 1.5 V versus Zn/Zn^{2+}, while maintaining the same Zn utilization, could achieve significantly higher power energy. The impact of the cell voltage on its energy density (based on the active materials) can be described as Equation (1):

$$E = \frac{Q_{cat} \times Q_{an}}{Q_{cat} + Q_{an}} \times \Delta V_{cell} \quad (1)$$

where Q_{cat} and Q_{an} represent the specific capacities of the active materials in the cathodes and anodes, respectively. ΔV_{cell} denotes the difference between the average operating potentials of these electrodes, establishing the cell's average discharge voltage.

-**Dissolution**: The dissolution of V-based cathodes in aqueous electrolytes is a prevalent issue (Figure 1b), convolutedly influenced by the water activity, electrolyte pH, and operating conditions (e.g., voltages and rates).[19,24] There are various soluble phases of V in aqueous electrolyte, such as VO^{2+}, V^{3+}, VOH^{2+}, V^{2+}, $H_2VO_4^-$, and $HV_2O_5^-$.[25] V species dissolution is a spontaneous process with Gibbs free energy (ΔG) <0, which can also occur when the battery is not assembled, mainly caused by the high polarity of free water.[26] For example, in most commonly used mild acidic electrolytes, the dissolution of V_2O_3 occurs as Equation (2):

$$V_2O_3 + 6\,H^+ + 9\,H_2O \leftrightarrow 2\,[V(H_2O)_6]^{3+}$$
$$\leftrightarrow 2\,[V(H_2O)_{6-x}(OH)_x]^{(3-x)+} + 2x\,H^+ \quad (2)$$

© 2024 The Author(s). Advanced Energy Materials published by Wiley-VCH GmbH

16146840, 2024, 31, Downloaded from https://advanced.onlinelibrary.wiley.com/doi/10.1002/aenm.202401704 by University of Adelaide Alumni, Wiley Online Library on [02/04/2025]. See the Terms and Conditions (https://onlinelibrary.wiley.com/terms-and-conditions) on Wiley Online Library for rules of use; OA articles are governed by the applicable Creative Commons License

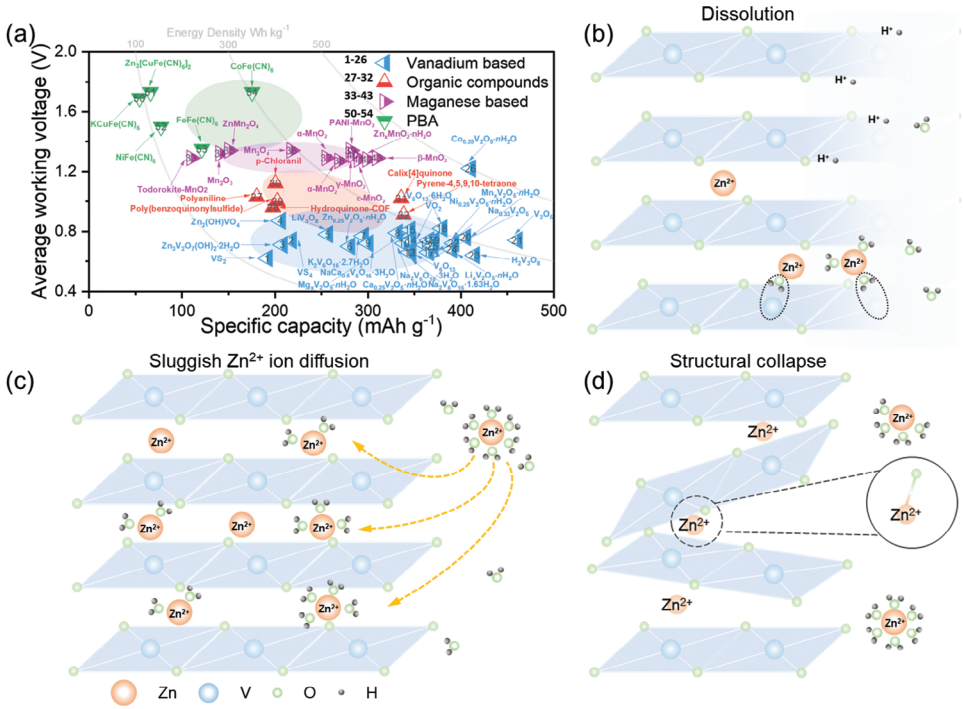


Figure 1. a) Comparison of typical working voltages of different cathodes. Numbers 1–26 correspond to V-based materials, 27–32 relate to organic compounds, 33–43 represent Mn-based materials, and 50–54 are associated with PBA-based materials. Schematics of challenges of V-based cathodes including b) dissolution, c) sluggish Zn2+ ion diffusion, and d) structural collapse.

Beyond the electrolytic environment's influence on V dissolution, recent theoretic simulations have shown that intercalated hydrated Zn^{2+} ions create large cavities within the cathode lattice.[24c] These conditions facilitate the coordination of co-intercalated free water molecules with partially coordinated V, thereby accelerating V dissolution. Dissolution process not only reduces capacity but also leads to the formation of a passivating layer.[24d,27] For instance, under conditions where pH < 3.2 and $[V^{5+}] < 10^{-1}$ M (pH dependent), VO^{2+} becomes the most stable V species in aqueous solution. Continuing the dissolution progresses, the consumption of protons causes a localized increase in pH, transforming VO^{2+} into $VO_2(OH)_2^-$ (or $H_2VO_4^-$).[25b] This transformation facilitates further reactions with Zn^{2+} in the electrolyte to form passivating layer ZVO ($Zn_3V_2O_7(OH)_2{\cdot}2H_2O$). Moreover, the dissolved V species can migrate through the separator and deposit on the anode, thereby impeding the reversible plating and stripping of Zn^{2+} ions. In general, these problems exacerbate more seriously at low current densities.

-**Sluggish Zn^{2+} transport kinetics, structure collapse, and strong electrostatic interactions**: In aqueous electrolyte systems, the divalent Zn^{2+} possesses strong Columbic interaction with highly polar water molecular to form $[Zn(H_2O)_6]^{2+}$ ions, which incur high desolvation penalty at electrode-electrolyte interface and sluggish Zn^{2+} ion transportation (Figure 1c). Besides, V-based cathodes possess intrinsic inferior electronic conductivity which obstructs the smooth migration. With the insertion of Zn^{2+}, the structure stability of V-based cathode is under challenge since the competition between V—O and Zn—O bonds. This issue is magnified by the periodic expansion and contraction of the lattice during the ion insertion and extraction processes, which inflicts mechanical stress and leads to structural pulverization (Figure 1d).[28] The delicate nature of these materials, bound by weak van der Waals forces, further heightens the risk of structural collapse. Compounding these challenges are the strong electrostatic interactions between the Zn^{2+} ions and the V-based cathode structure. The significant charge density of Zn^{2+} ions induces a pronounced polarization effect, potentially disrupting the lattice's electroneutrality during discharge and leading to severe lattice deformation. This deformation not only hinders efficient ion storage and movement but also creates physical barriers that limit the availability of storage sites for Zn^{2+} ions. Such barriers contribute to the capacity decay and reduced rate performance, underscoring the need for innovative solutions to overcome these interrelated issues for the successful development of AZIB technology.[4c,29]

3. Defect Engineering on Vanadium-Based Cathode Materials

3.1. Defect Types and Their Effects

According to the second law of thermodynamics, a certain amount of disorder or defects is unavoidable in crystalline materials. No crystals have perfect periodicity but frequently contain a substantial number of structural irregularities caused by compositional inhomogeneities, known as defects.[30] To achieve thermodynamically less soluble and thus more stable electrode materials, understanding and controlling defects have become

© 2024 The Author(s). Advanced Energy Materials published by Wiley-VCH GmbH

16146840, 2024, 31, Downloaded from https://advanced.onlinelibrary.wiley.com/doi/10.1002/aenm.202401704 by University of Adelaide Alumni, Wiley Online Library on [02/04/2025]. See the Terms and Conditions (https://onlinelibrary.wiley.com/terms-and-conditions) on Wiley Online Library for rules of use; OA articles are governed by the applicable Creative Commons License

crucial pathways to practical application, leading to the burgeoning field of defect engineering. Defect engineering is the art of manipulating the type, concentration, and spatial distribution of defects within crystal structures to optimize their electronic structure, charge transfer, ion transport behaviors, and to provide more active sites for guest ions. As discussed above, the defect structure in crystals includes point, line, plane, and volume defects. Among them, point defects are the main content of defect chemistry research. Point atomic level defects, mainly composed of lattice vacancies or ionic doping.[31] Vacancies refer to the positions of the lattice that are not occupied by atoms, here mainly refer to the oxygen vacancy and cation vacancy. Typically, the existence of vacancies will not affect the composition or stoichiometry of the entire crystal but do affect the atoms around the vacancies, causing local lattice relaxation. Ionic doping mainly involves cations/anions entering the crystal lattice to alter the original atomic arrangement, inducing partial lattice distortion and leading to charge redistribution and changes in electronic structures.

Of significant advances only in recent years, the intercalation of water molecules into cathode crystal was corroborated to directly affect the structure of cathode material, manipulating ion migration behaviors and electronic structures. Meanwhile, amorphization of electrode materials is often regarded as one of the "original sins" that cause battery capacity degradation, given the collapse of the ordered crystal space structure damages the originally ordered Zn^{2+} ion storage sites. Interestingly, some special amorphous materials have been reported to break the limitations of the original ordered crystal structure and establish new ion diffusion channels, providing a disordered framework for ion storage that delivers better performance than their crystalline counterparts.

In this chapter, we will highlight the advancement of defect engineering strategies in developing efficient and durable V-based electrode materials for AZIBs. Key categories are divided based on the defect types: 1) oxygen vacancy, 2) cation vacancy, 3) cationic doping, 4) anionic doping, 5) water intercalation, and 6) lattice disorder (amorphization). A few significant works will be exemplified in each section.

3.1.1. Oxygen Vacancy

Oxygen vacancy (V_O) is a structural defect formed by removing part of oxygen atoms in the crystal lattice of V-based materials. Due to its low formation energy, V_O is one of the most common and important defects, which could operatively tailor the physical and chemical properties of V-based cathode materials without significantly altering the lattice.[32] This indicates that the introduction of V_O into inherently stable crystal structures does not lead to a significant decrease in stability or create issues like dissolution. As a result, these electrode materials, less prone to dissolution, can achieve faster reversible adsorption/desorption of Zn^{2+} ions. For instance, Peng et al. reported that V_O could affect Zn^{2+} ion adsorption behaviors in V_6O_{13}.[33] Density functional theory (DFT) simulation results revealed that the introduction of V_O can lead to a thermoneutral Gibbs free energy of Zn^{2+} ion adsorption(ΔG_{Zn2+}), conductive to reversible Zn^{2+} ion adsorption/desorption (**Figure** 2a). By contrast, the ΔG_{Zn2+} of pristine V_6O_{13} was markedly more negative, indicating much stronger adsorption of Zn^{2+} that hampered the Zn^{2+} desorption, obscured the electrochemically active surface areas, and ultimately impaired cycle performance.[34] Moreover, the modulation of Zn^{2+} ion storage/release mechanisms was studied by surface electron density difference analysis (Figure 2b). Different from the pristine V_6O_{13} that possesses uniform charge distribution, electrons accumulated around the oxygen-deficient site of V_6O_{13}. Spare electrons were left over after the extraction of oxygen atoms, which can subsequently contribute to the delocalized electron cloud of the oxygen-deficient V_6O_{13}, hence enhancing the intracrystal reversible capacity. Based on the significantly enhanced Zn^{2+} ion diffusion coefficient and capacity of oxygen-deficient V_6O_{13}, they postulated that the oxygen-deficient structure might enable dual-direction Zn^{2+} ion insertion via both the conventional path (i.e., along *ab* plane) and the newly created road by V_Os (along *c* axis) (Figure 2c). This shows the possibility of further controlling linear or planar defects through the management of point defects. Therefore, in addition to the optimization of Zn^{2+} ion diffusion by tailoring ΔG_{Zn2+}, the structural deformation (i.e., tunnel expansion, and dislocation) resulting from V_O can also optimize the Zn^{2+} ion diffusion process. In another work, Cao et al. synthesized an oxygen-deficient VO_2 nanobelt. The X-ray diffraction (XRD) pattern shift and lattice parameters calculated via DFT revealed that the introduction of V_Os increases the lattice constants *a* and *c*, corresponding to the expansion of *b* tunnels, speeding up ion diffusion and ameliorating electrochemical performance.[32c] In their following work, it was observed that the existence of V_O could lead to the skewing of other adjoin atoms and form dislocation (Figure 2d,e).[35] As a consequence, the enlarged interplanar distance of V_O-containing $Na_{0.76}V_6O_{15}$/PEDOT (PNVO) can facilitate the diffusion of Zn^{2+} ion and weaken the electrostatic interactions, thereby improving the cathode's rate performance and cycling stability.

The kinetics of electrochemical reactions are often limited by the slower process of either ion diffusion or electron transfer, electrode materials are typically required to possess both a high ionic diffusion coefficient and high electrical conductivity. In addition to improving Zn^{2+} diffusion, as previously mentioned, some groups have found that the introduction of V_Os can enhance the ionic conductivity of the cathode.[32c,36] Based on the theoretical calculations, Parkin and co-workers studied the projected density of states (PDOS) and the total density of states (TDOS) of $NH_4V_4O_{10}$ with and without V_Os (Figure 2f).[37] The narrowing of the bandgap and the shift of the Fermi energy level reveal that the electronic conductivity increased after the inclusion of V_Os. Correspondingly, by comparing the spin density of pristine and oxygen-deficient $NH_4V_4O_{10}$, they concluded that localized electrons will be generated on the additional two V sites adjacent to the V_O site in the defective $NH_4V_4O_{10}$. The electrons can diminish the total energy to maintain structural integrity during cycling while promoting the reversible deintercalation of Zn^{2+} ions with thermoneutral ΔG. The authors also compared the minimum energy migration path of Zn^{2+} ions in the two samples and confirmed that V_Os benefit Zn^{2+} ions mobility by lowering the energy barrier from 0.82 to 0.58 eV (Figure 2g). Accordingly, the dual effects of V_Os on Zn^{2+} ion diffusion and conductivity effectively boost the reversibility of the Zn^{2+} ions

© 2024 The Author(s). Advanced Energy Materials published by Wiley-VCH GmbH

16146840, 2024, 31, Downloaded from https://advanced.onlinelibrary.wiley.com/doi/10.1002/aenm.202401704 by University of Adelaide Alumni, Wiley Online Library on [02/04/2025]. See the Terms and Conditions (https://onlinelibrary.wiley.com/terms-and-conditions) on Wiley Online Library for rules of use; OA articles are governed by the applicable Creative Commons License

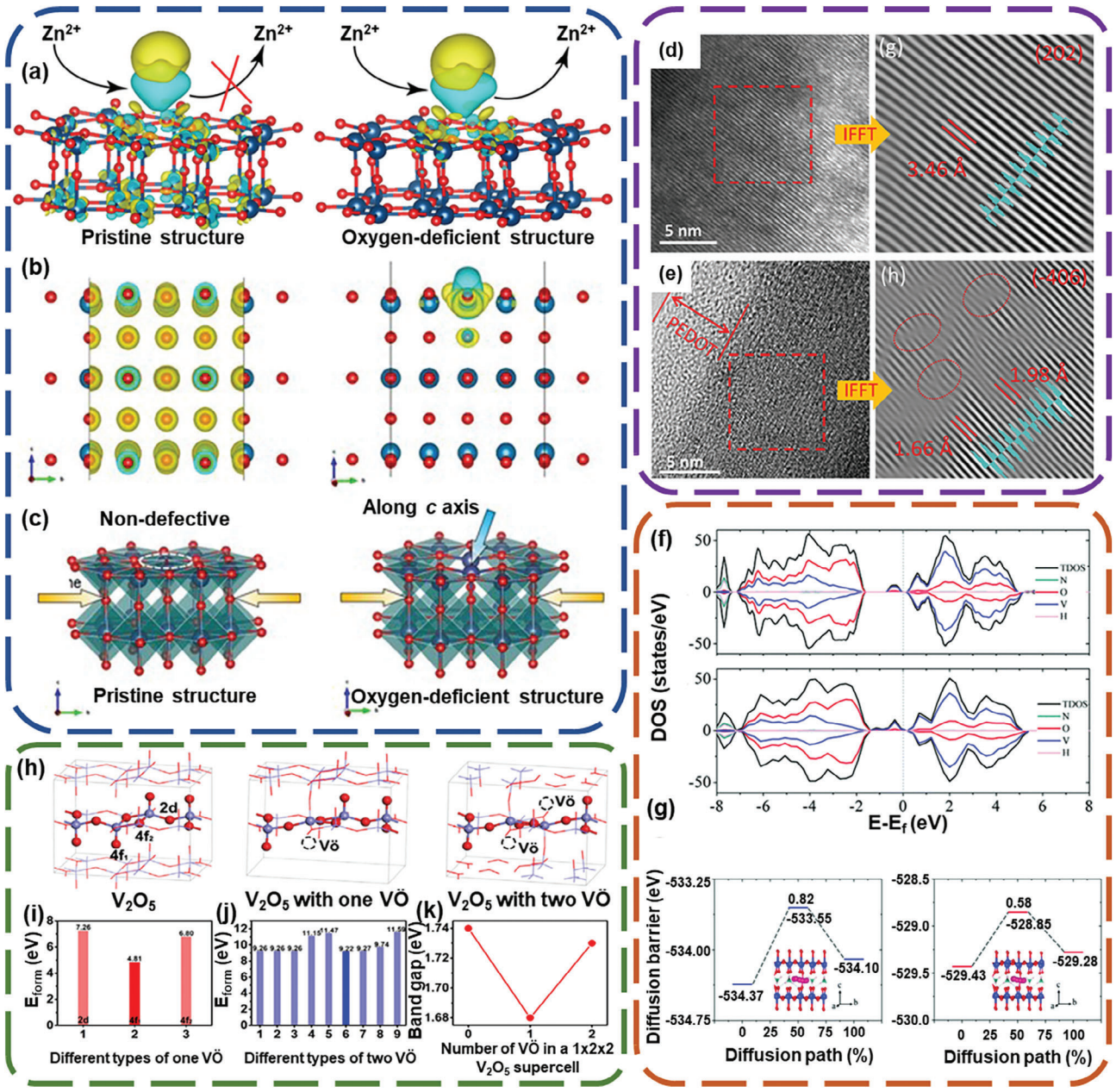


Figure 2. a) Charge density and schematic illustrations for Zn^{2+} storage/release for the V_6O_{13} and oxygen-deficient V_6O_{13} b) Charge distribution of the V_6O_{13} and oxygen-deficient V_6O_{13} c) Material Structure and related Zn^{2+} diffusion/insertion paths. Reproduced with permission.[33] Copyright 2019, Wiley-VCH. d,e) High-resolution transmission electron microscopy (HRTEM) and corresponding Inverse Fast Fourier Transform (IFFT) images of the NVO and V_O-PNVO. Reproduced with permission.[35] Copyright 2021, Elsevier. f) The projected density of states (PDOS) and the total density of states (TDOS) of the $NH_4V_4O_{10}$ (top) and oxygen-deficient hydrated $NH_4V_4O_{10}$ (bottom) g) The diffusion barrier and minimum energy migration pathway of Zn^{2+} in the $NH_4V_4O_{10}$ (left) and oxygen-deficient hydrated $NH_4V_4O_{10}$ (right). The spheres in blue, red, green, and light pink color represent V, O, N, Zn, and H, respectively. Reproduced with permission.[37] Copyright 2020, The Royal Society of Chemistry. h) The structure of V_2O_5 and oxygen-deficient V_2O_5 (containing one or two VÖ). The spheres in purple, and red color represent V and O, respectively. i) The formation energy (E_{form}) of the first V_O in V_2O_5. j) The E_{form} of the second V_O in V_2O_5 in 4f1 – V_O – V_2O_5. k) The bandgap of V_2O_5, 4f1 – V_O – V_2O_5, (containing one V_O), and 6 – V_O – V_2O_5 (containing two V_Os). Reproduced with permission.[39] Copyright 2021, Springer Nature.

insertion/extraction process, thereby improving the capacity and rate performance.[37] Similar conclusions were drawn in other V-based materials with diverse crystal structures, such as $K_2V_8O_{21-x}$ and $NH_4V_3O_8$, albeit in a different order to promote the electrochemical activities.[38]

While V_O presents essential boosting effects in several electrochemical properties of V-based materials, one critical question rises as whether these promoting effects are always proportional to the concentration of these vacancies. The response to this query is negative. Sun et al. investigated the effect of

© 2024 The Author(s). Advanced Energy Materials published by Wiley-VCH GmbH

16146840, 2024, 31, Downloaded from https://advanced.onlinelibrary.wiley.com/doi/10.1002/aenm.202401704 by University of Adelaide Alumni, Wiley Online Library on [02/04/2025]. See the Terms and Conditions (https://onlinelibrary.wiley.com/terms-and-conditions) on Wiley Online Library for rules of use; OA articles are governed by the applicable Creative Commons License

V_O concentrations on the structural and electronic properties of V_2O_5.[39] The formation energy (E_{form}) of V_O on different locations are enumerated to configure the smallest energy configurations of oxygen-deficient free, one V_O, and two V_O containing V_2O_5 (denoted as V_2O_5, $4f_1 - V_O - V_2O_5$, and $6 - V_O - V_2O_5$) (Figure 2h–j). Analysis from the PDOS clarifies that with an increasing concentration of V_O, the energy gap initially narrows before subsequently widening (Figure 2k). This phenomenon implies that the conductivity of oxygen-deficient V_2O_5 does not maintain a direct proportionality with the concentration of V_O. Consequently, a comprehensive understanding of the formation mechanism of oxygen deficits and their structural implications becomes paramount. In this context, Dou et al. have studied the formation mechanism of V_O.[1b] In situ electron paramagnetic resonance (EPR) and XRD analyses revealed that below 240 °C, the creation of oxygen-deficient sites is primarily due to minor alterations in the interlayer structure and the removal of lattice water, leading to the distortion of the V—O layer. Beyond 260 °C, the diffraction peaks associated with (001) planes vanish, pointing to the disintegration of the interlayer structure and triclinic lattice due to the continuous loss of interlayer lattice water. Excessively high concentrations of V_O could precipitate the disintegration of interlayer structures and the degradation of the crystal lattice, adversely affecting the material's structural integrity and electrochemical efficacy. Therefore, introducing an optimal amount of V_O into V-based materials can promote Zn^{2+} transport kinetics while maintaining crystal stability. Such enhancements encourage a higher reversible capacity and optimize the material's conductivity, thereby contributing to the development of high-performance AZIBs.

3.1.2. Cation Vacancy

In a crystal compound, if a cation is absent from a lattice site, that defect is called a cation vacancy. Compared with V_O, the cation vacancy is much less discussed in existing literatures. Theoretically, the introduction of cation vacancies can alleviate the high repulsive forces within the lattice. This is particularly beneficial in mitigating the issue of slow diffusion of divalent Zn^{2+} ions in the cathode lattice. In general, the mobility of ion diffusion is commonly described by the ion diffusion coefficient (D). D can be written in the following manner:[40]

$$D = \rho\lambda^2\Gamma \tag{3}$$

ρ refer to the geometric factor that depends on the sublattice symmetry of the interstitial sites, and λ is the hop distance between adjacent interstitial sites. As Vineyard deduced in the classical limit, the hop frequency (Γ) can be approximated as[41]

$$\Gamma = \nu^* \exp\left(\frac{\Delta E}{kT}\right) \tag{4}$$

ν^* refer to vibrational factor derived in the classical limit of the Harmonic approximation, ΔE is ion migration barrier, k is Boltzmann constant, and T is temperature. It is well established that the presence of suitable crystal defects, like impurities and vacancies in the cathode material, can result in a reduction in ΔE. As demonstrated by the preceding equation, D and ΔE are exponentially related, a modest drop in ΔE induced by crystal defects can result in a substantial rise in the ion diffusion coefficient. Hence, by creating cation vacancies, the lattice can become more adaptive to the movement of Zn^{2+} ions, thereby enhancing ion transport and overall electrochemical performance.

For V-based materials, the V vacancy (V_V) is the most possible cation defect given the abundance of V in the material matrix. Chou et al. used DFT calculations to elucidate the impact of V vacancies on the potential Zn^{2+} intercalation behavior in Zn-V_2O_3 electrolytic batteries.[32b] By comparing Zn^{2+} intercalation energies across models containing varying levels of vacancies, they observed that as the level of cation vacancies increased from 1 to 4, the Zn^{2+} intercalation energy decreased from 2.06 to −0.72 eV. This finding indicates that the V_2O_3 featuring V_Vs is thermodynamically advantageous for the insertion of Zn^{2+} ions. Furthermore, the V_Vs can provide reversible intercalation site for Zn^{2+} ion accommodation, contributing to higher capacities and a more stable structure against collapsing during cycling. Song et al. reported that V-deficient (V_d) V_2O_3, containing ≈5.7% defect concentration, exhibited remarkable cycling stability.[15c] After 30000 cycles at 5 A g^{-1}, the assembled battery maintained ≈81% of its capacity. Such exceptional cycle stability is postulated to arise from the profusion of vacancy clusters, which mitigate the pronounced electrostatic interactions between Zn^{2+} ions and the V_d-V_2O_3 matrix. DFT calculations (**Figure 3a,b**) showed that the defect-free V_2O_3 has a positive ΔG, suggesting the intercalation of Zn^{2+} ions into the matrix is thermodynamically difficult. On the contrary, after initial discharging, V_d-V_2O_3 underwent a self-optimization process, leading to a Zn-doped V_d-V_2O_3 structure where Zn^{2+} can be reversibly inserted or extracted in subsequent cycles.

Apart from V vacancies, the construction of corresponding cation vacancies in V-based materials containing other cations offers diverse alternatives. Cao et al. described a modified $NH_4V_4O_{10}$ in which partial removal of NH_4^+ ions resulted in an increased interlayer spacing (Figure 3c).[29] This modification created more active sites, enhancing diffusion pathways, and making the insertion/extraction of Zn^{2+} ions more efficient. Furthermore, it alleviated cycling degradation due to the decreased dissolution of ammonium ions throughout the cycles. The cycling performance (Figure 3d) of the NH^{4+}-deficient $NH_4V_4O_{10}$ is impressive compared to the defect-free counterpart (81% vs ≈40% capacity retention after 1000 cycles at 2 A g^{-1}).

3.1.3. Cationic Doping

In the process of steering V-based materials towards practical applications using diverse and multi-faceted defect engineering approaches, ion doping strategies represent an "addition" modification of material properties, in contrast to the "subtraction" approach of introducing vacancies to enhance conductivity and Zn^{2+} transport kinetics in crystal materials.

In ion doping strategies, cationic doping can be categorized into two types: substitutional doping and interstitial doping. Among these, substitutional type cationic doping refers to the introduction of cations (such as NH_4^+, Na^+, K^+, Ca^{2+}, and Zn^{2+}) to replace the original cations (mostly V) and occupy their

© 2024 The Author(s). Advanced Energy Materials published by Wiley-VCH GmbH

16146840, 2024, 31, Downloaded from https://advanced.onlinelibrary.wiley.com/doi/10.1002/aenm.202401704 by University of Adelaide Alumni, Wiley Online Library on [02/04/2025]. See the Terms and Conditions (https://onlinelibrary.wiley.com/terms-and-conditions) on Wiley Online Library for rules of use; OA articles are governed by the applicable Creative Commons License

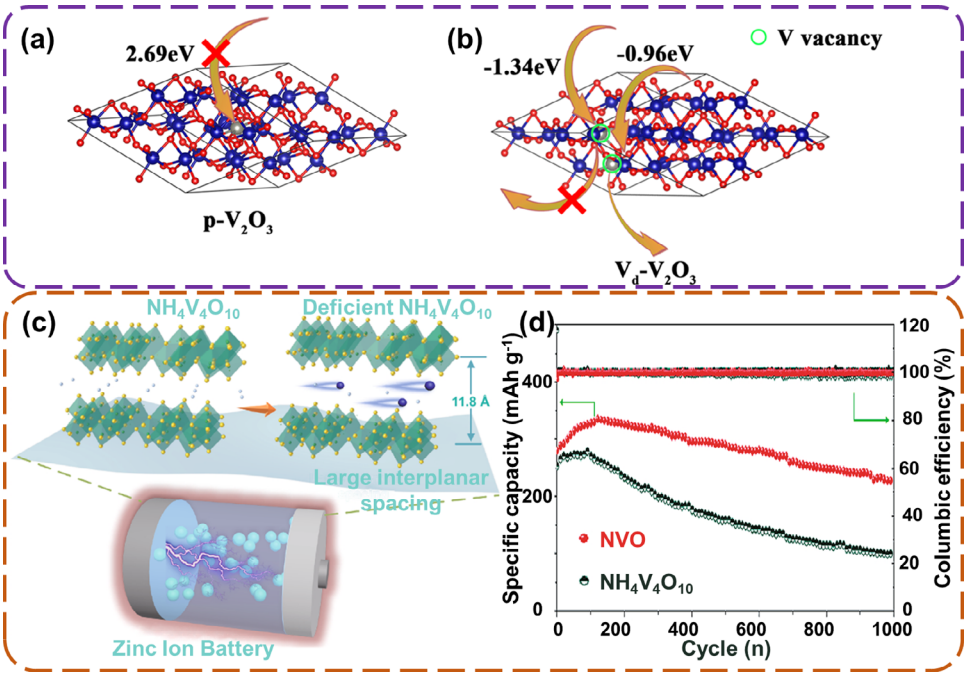


Figure 3. The DFT calculation of Zn^{2+} intercalation Gibbs free energy according to a) pristine V_2O_3 (p-V_2O_3) and b) V_d–V_2O_3 model. Reproduced with permission.[15c] Copyright 2021, Springer Nature. c) The diagram of NH^{4+}-deficient in $NH_4V_4O_{10}$ benefits the expanded interplanar space. d) Cycling performance of $NH_4V_4O_{10}$ and cationic defect NVO at 2 A g^{-1}. Reproduced with permission.[42] Copyright 2021, Springer Nature.

lattice sites, whereas interstitial doping is to introduce cations into previously unoccupied sites. Generally, most published research on cation doping in V-based cathodes focuses on interstitial doping. The effects of this doping are primarily manifested in three key aspects: optimizing Zn^{2+} ion diffusion kinetics, enhancing electrode material stability, and elevating the cathode potential.[43] It is known that restricted ion diffusion paths significantly contribute to the degradation of performance, since limitations in carrier diffusion during reactions can lead to considerable structural deformation and irreversible reactions.[43] The pre-intercalated cations act as "pillars", which expand the interlayer space, thereby improving the structural stability as well as electrical conductivity of the material. Of the three impacts from cation doping, the former two (viz., optimizing ion kinetics and enhancing material stability) are particularly crucial for fulfilling the demands of grid energy storage systems that require exceptionally long cycle stability. Here, several representative works are exemplified to clarify the far-reaching influence of cation doping in different types of V-based cathode materials.

Zn^{2+} Ion Kinetics Optimization: Cationic doping, which involves the introduction of impurity cations into crystal material, has been verified to be efficient in promoting electronic conductivity since this type of defect can decrease the electron transition energy. Additionally, by applying interstitial impurities, the charge compensation effect can partially shift transition metals to mixed-valence states, consequently altering the electrical conductivity of materials.[15a] Li et al. reported an interlayer Mn^{2+}-doped hydrated layered vanadium oxide ($Mn_{0.15}V_2O_5{\cdot}nH_2O$) synthesized via a microwave-assisted strategy. DFT calculation (**Figure 4a**) reveals that Mn^{2+} doping can modify the interlayer charge of V_2O_5.[44] The comparison of band structures (Figure 4b) of the pristine V_2O_5 and $Mn_{0.15}V_2O_5{\cdot}nH_2O$ shows that the Mn^{2+} doping can narrow the bandgaps from 2.28 to 0.9 eV, leading to an increase in conductivity. The computed PDOS (Figure 4c) results indicate that with the doping, a new energy level near the Fermi level emerged, which also implies the significant increase in conductivity. In the prospect of material structure, cationic doping can enlarge ion diffusion channels and weaken Zn—O bonds, resulting in optimization of Zn^{2+} ion kinetics.[45] Cao's group reported Mn^{2+} expanded hydrated vanadate (MnVO) materials that delivered a high specific capacity of 415 mAh g^{-1} at 0.5 A g^{-1}, along with good rate performance.[45] Such enhancement was attributed to the increased interlayer space (Figure 4d) created by the Mn^{2+} ions and embedded water molecules, where the positively charged Mn^{2+} ion forms chemical intercalation with terminal oxygen from the [VO_n] layers. Wang et al. studied the effects of Na- and Mn- co-pre-insertion to V_8O_{20}, and they concluded that the inserted Mn^{2+}/Mn^{3+} attributed to the improvement of electronic conductivity, while the Na^+ facilitated the migration of Zn^{2+} ions.[46] The effects of pre-intercalate transition metal ions (Fe^{2+}, Co^{2+}, Ni^{2+}, Mn^{2+}, Zn^{2+}, and Cu^{2+}) on the structural stability, electrical conductivity, and ion diffusion kinetics of V_2O_5 were investigated comprehensively by Zhou's group.[47] It is demonstrated that the introduction of metal ions into the V_2O_5 interlayer not only greatly enhances the ion diffusion ability due to the improved layer spacing and electrical conductivity, but also the strategy has a certain universality that can be applied to other material systems to overcome its drawbacks. Not surprisingly, the cation doping strategy also applies to other V-compounds. For example, Zheng et al. use Co^{2+} doping to reduce the interfacial attraction of VS_4 interlayer to Zn^{2+}.[48] The widened interlayer distance accompanied with the surface charge rearrangement in

© 2024 The Author(s). Advanced Energy Materials published by Wiley-VCH GmbH

16146840, 2024, 31, Downloaded from https://advanced.onlinelibrary.wiley.com/doi/10.1002/aenm.202401704 by University of Adelaide Alumni, Wiley Online Library on [02/04/2025]. See the Terms and Conditions (https://onlinelibrary.wiley.com/terms-and-conditions) on Wiley Online Library for rules of use; OA articles are governed by the applicable Creative Commons License

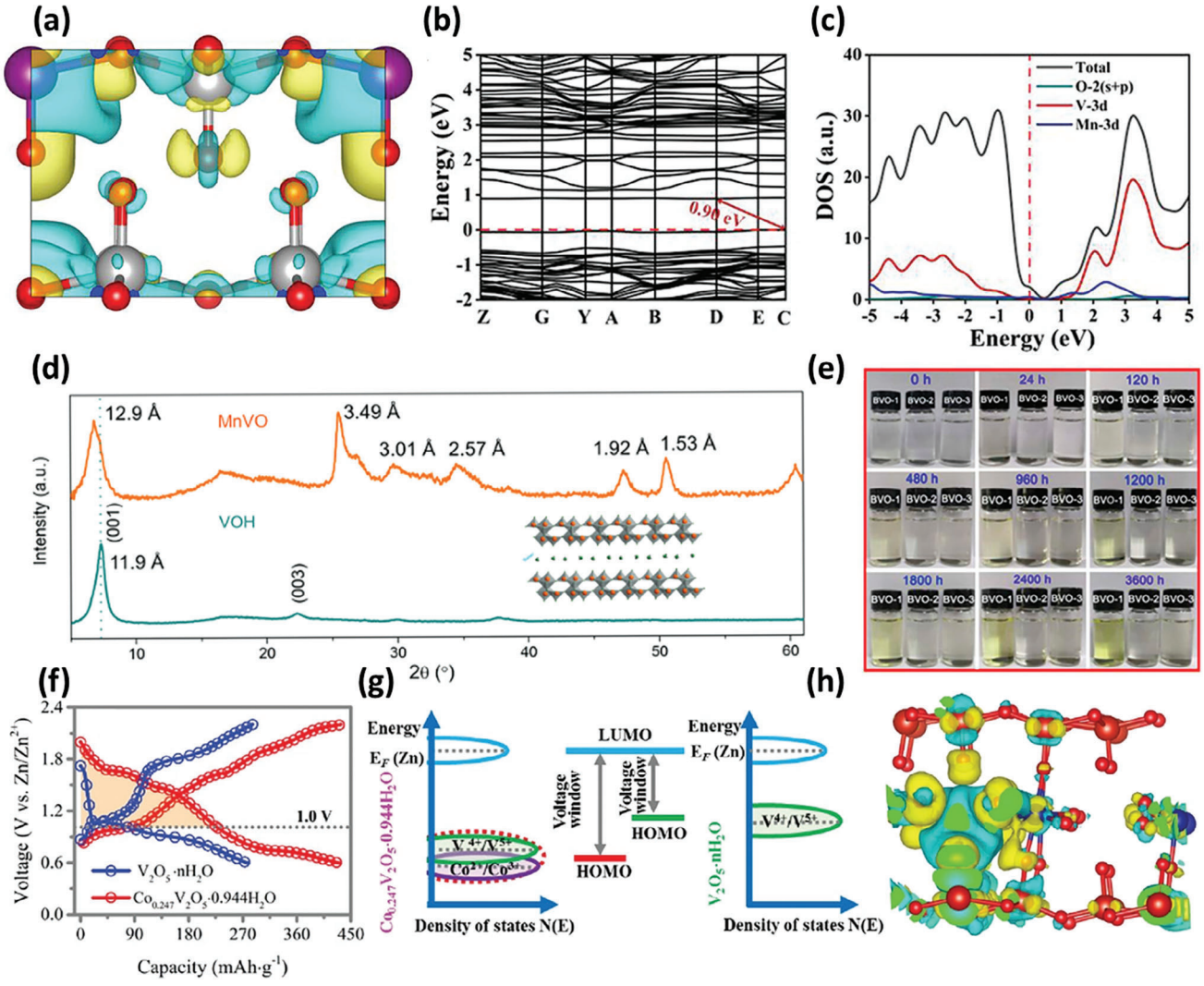


Figure 4. a) The electron density difference of Mn^{2+}-doped V_2O_5. The spheres in red, purple, and silver represent oxygen atoms, manganese atoms, and vanadium atoms, respectively. Charge accumulation is depicted in yellow, whereas depletion is depicted in blue b) The total band structure of Mn^{2+}-doped V_2O_5 c) The PDOS of Mn^{2+}-doped V_2O_5. Reproduced with permission.[44] Copyright 2019, Wiley-VCH. d) The XRD patterns of pristine hydrated vanadium pentoxide (VOH) and Mn (II) cation expanded hydrated vanadium pentoxide (MnVO). Reproduced with permission.[45] Copyright 2019, Royal Society of Chemistry. e) The images of static soaking Ba^{2+} ions dopped V-based electrodes in 2 M $ZnSO_4$ for different durations. Reproduced with permission.[60] Copyright 2020, American Chemical Society. f) Galvanostatic charge/discharge curves of $Co_{0.247}V_2O_5{\cdot}0.944H_2O$ and $V_2O_5{\cdot}nH_2O$ g) comparison graph of energy and DOS. h) The charge distribution change after Zn^{2+} ion inserted $Co_{0.247}V_2O_5 \cdot 0.944H_2O$ framework. The cyan, and yellow color represent the charge decrease and increase, respectively. Reproduced with permission.[63] Copyright 2019, Wiley-VCH.

the modified VS_4 enhances the charge shielding of Zn^{2+}, thus accelerating the transport of ions and electrons.

Improved Electrode Material Stability: AZIBs' cycle stability is highly correlated with the cathode structural stability. Structure collapse and V dissolution have become key adverse factors that result in limited battery lifespan and capacity degradation. In 2016, Nazar et al. reported a bilayer red vanadium oxide bronze ($Zn_{0.25}V_2O_5{\cdot}nH_2O$), where the indigenous Zn^{2+} ions play the role of the pillar to stabilize the layer structure during cycling.[49] Inspired by this work, numerous V-based cathodes with stabilizing doping metal cations have been reported, such as $Li_xV_2O_5{\cdot}nH_2O$,[50] $Na_{0.33}V_2O_5$,[51] $K_{0.25}V_2O_5$,[52] Co^{2+} doped $(NH_4)_2V_{10}O_{25}{\cdot}8H_2O$,[53] $CaV_6O_{16}{\cdot}3H_2O$,[54] $Mn_{0.15}V_2O_5{\cdot}nH_2O$,[44] δ-$Ni_{0.25}V_2O_5{\cdot}nH_2O$,[55] $Sn_{1.5}V_2O_7(OH)_2{\cdot}3.3H_2O$.[56] Wang et al. developed a substitutional Al-doped $V_{10}O_{24}{\cdot}12H_2O$ host, where the dopped Al^{3+} can form strong Al—O bonds to prevent the structure collapse.[57] Benefiting from the improved structure stability, the assembled battery delivered superior cycling performance of 3000 cycles at 5 A g^{-1} with 98% capacity retention.

As previously mentioned, one core issue affecting the practical application of V-based materials is their severe dissolution in aqueous electrolyte systems, especially at low current densities. The dissolution of V-based materials in aqueous electrolytes is a spontaneous reaction process because of the strong polarity of water molecules.[58] This problem will not only lead to the

© 2024 The Author(s). Advanced Energy Materials published by Wiley-VCH GmbH

16146840, 2024, 31, Downloaded from https://advanced.onlinelibrary.wiley.com/doi/10.1002/aenm.202401704 by University of Adelaide Alumni, Wiley Online Library on [02/04/2025]. See the Terms and Conditions (https://onlinelibrary.wiley.com/terms-and-conditions) on Wiley Online Library for rules of use; OA articles are governed by the applicable Creative Commons License

degradation of battery capacity, but also have a negative impact on the cyclability of the battery because the dissolved metal ions will be deposited on the electrode to form a passivation layer.[59] Cationic doping has been proven an effective method that mitigates this dissolution issue. For example, Xiong et al. reported the introduction of Ba^{2+} ions into V_3O_8 type and V_2O_5 type cathodes can tackle the dissolution issue along with the elimination of $Zn_4SO_4(OH)_6{\cdot}xH_2O$ precipitates.[60] As can be observed from the static soaking experiment (Figure 4e), the $Ba_{1.2}V_6O_{16}{\cdot}3H_2O$ sample exhibited ultra-high stability after soaking at 2 M $ZnSO_4$ electrolyte for more than 3600 h. Similarly, the pre-intercalation of NH_4^+ ions works but they can provide a higher gravimetric and volumetric energy density due to their low weight. Liang et al. reported an AZIB with NH_4^+ ions embedded $V_4O_{10}nH_2O$ cathode, where the NH_4^+ ions play a crucial role in guaranteeing cycling stability and offering an impressive energy density (374.3 Wh Kg^{-1}) as well as power density (9000 W Kg^{-1}).[61] Zhang et al. discovered the co-intercalation of Cs^+ and Na^+ ions into vanadium oxide bronze ($Na_{0.33}Cs_{0.03}V_2O_5$) nanowires also leads to a stable cathode (capacity retention over 93% for 1000 cycles in 2 M $ZnSO_4$ aqueous solution) with negligible dissolution issues.[62]

Elevated Operation Voltage: The working voltage of V-based cathodes in AZIBs is typically low, and generally ≈80% of the capacity contribution is attributable to electrochemical reactions occurring below 1.0 V (vs Zn). This will substantially compromise the energy density of V-based AZIBs, despite the cathode's high specific capacity. The introduction of redox couple with higher potential into the cathode materials via cationic doping is an effective method to elevate the working voltage.[64] Across the synergistic effect of Co^{2+} ions doping and utilization of a "water-in-salt" electrolyte, Zhi's group successfully developed a high-voltage output (1.7 V) AZIBs.[63] It is worthwhile to note that 52.54% of the total capacity of $Co_{0.247}V_2O_5{\cdot}0.944H_2O$ cathode can be attributed to the electrochemical reactions occurring above 1.0 V (Figure 4f). Further analyses (Figure 4g,h) suggest that the interaction between the Co-3d and V-3d orbitals in the material increases the redox potential of V^{5+}/V^{4+}; due to the p-d hybridization between Co-3d, V-3d, and O-2p orbitals, the effective charge of inserted Zn^{2+} ions decreased from 2 to 1.35 which enable a high mobility of Zn^{2+} ions.

In the current context of technological urgency, while increasing the working voltage might not seem as immediate a priority as enhancing electrode stability, achieving higher energy density remains the ultimate development goal in screening efficient electrode materials. However, research on cation substitution is still in a nascent stage, with detailed mechanisms of improvement remaining unclear. Focusing on doping elements that stabilize the electrode structure and improve longevity without significantly compromising other key performance metrics is crucial for advancing toward practical and efficient AZIB technologies.

3.1.4. Anionic Doping

Similar to cationic doping, anionic doping can also be effective in improving the working voltage. The $Na_3V_2(PO_4)_3$ electrode material of the NASICON structure was used for the first time by Huang et al. to store divalent ions in 2016.[65] The electrode material of the NASICON structure has a stable framework. In addition, due to the inducing effect, its redox voltage is higher than that of binary oxide analogues. In Huang's work, at 0.5 C, $Na_3V_2(PO_4)_3$/C composites deliver a reversible capacity of 97 mAh g^{-1} accompanied by a high discharge voltage ≈1.1 V. Jiang et al. introduced F^- species that have strong electronegativity into the NASICON structure and successfully increased the working voltage of $Na_3V_2(PO_4)_2F_3$ to 1.62 V.[65a] This method not only increases the energy density of the batteries but also leverages the stability of the NASICON structure to support sustained performance over multiple charge/discharge cycles. Despite so, in contrast to cationic doping, only a few studies have been conducted on anionic doping in V-based cathode materials. One possible reason for the comparatively rareness of bare anionic doping is that hetero anionic doping will concurrently introduce substantial V_Os, and the doping sites are prone to evolve (or leach away) during repeated charge/discharge cycles. As one pertinent example, Liang et al. reported that it is more likely the concomitant V_O sites that contributed to the expedited reaction kinetics in a phosphorus-doped V_2O_5 cathode.[66]

3.1.5. Water Intercalation

A very unique but often overlooked defect type is the intercalated water, which is always introduced during the synthesis of materials and/or subsequent operations in aqueous electrolytes. These embedded water molecules, like other intercalated ions, serve as "pillars" that directly expand the interlayer spacing and ensure structural stability of V-based cathodes, while avoiding the introduction of extra ions. It is well-known that the interlayer spacing of V_2O_5 is generally 4.4 Å, while the radius of hydrated zinc ions is 4.3 Å.[67] In scenarios where there are no embedding ions to widen the interlayer spacing, a constrained interlayer distance not only hampers Zn^{2+} ion diffusion but also under-utilizes the active sites of the cathode material. Consequently, the cathode may collapse due to continuous volume variations during charge/discharge cycles, deteriorating the battery's lifespan. Yang et al. highlighted that the existence of 1.29 structural water per V_2O_5 unit could enlarge the interlayer spacing to 12.6 Å.[68] Also, the existence of water molecules could affect the interlayer spacing during different electrochemical states via hydrogen bond formation among Zn^{2+}, $CF_3SO_3^-$, H_2O, and lattice oxygen. Simultaneously, the water-based shielding layer could contribute to the reduction of electrostatic bond strength, hence leading to a lower Zn^{2+} ion diffusion barrier and benefiting the cycling and rate performance (**Figure 5a,b**).

Apart from supporting the host framework, the "shielding effect" of intercalated water has been proven to reduce the "effective charge" of Zn^{2+} ions.[69] As the electrostatic strength formula indicates,

$$\propto \frac{1}{\epsilon_r r_0^2} \tag{5}$$

where the ϵ_r, and r_0 denote the permittivity of water, and the distance between the Zn^{2+} ion and the closest ions, respectively. The presence of water will increase the ϵ_r, and the enlarged interlayer spacing will increase the r_0, hence the electrostatic bond

© 2024 The Author(s). Advanced Energy Materials published by Wiley-VCH GmbH

16146840, 2024, 31, Downloaded from https://advanced.onlinelibrary.wiley.com/doi/10.1002/aenm.202401704 by University of Adelaide Alumni, Wiley Online Library on [02/04/2025]. See the Terms and Conditions (https://onlinelibrary.wiley.com/terms-and-conditions) on Wiley Online Library for rules of use; OA articles are governed by the applicable Creative Commons License

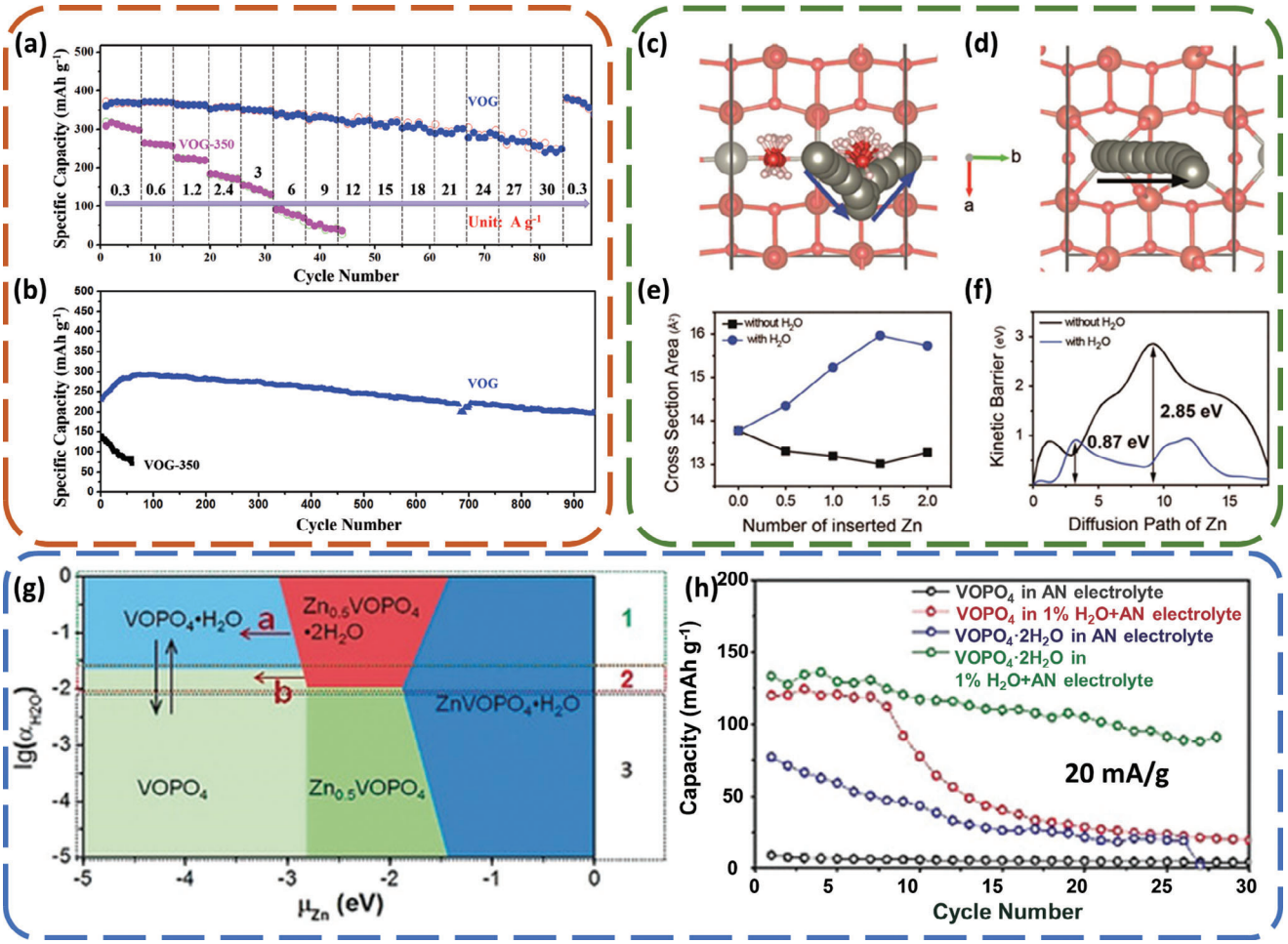


Figure 5. a) Rate performance and b) Cycling performance of $V_2O_5{\cdot}nH_2O$/graphene (VOG) and V_2O_5/graphene (VOG-350). Reproduced with permission.[68a] Copyright 2018, Wiley-VCH. Diffusion pathways of zinc ion c) with and d) without water. e) Cross section area change of different zinc ion intercalation states. f) Zinc ion diffusion barriers. Reproduced with permission.[70] Copyright 2019, Wiley-VCH. g) The phase diagram of $Zn_xVOPO_4{\cdot}nH_2O$ is determined based on the water activity and Zn chemical potential. h) The cycling performance of $VOPO_4$ with/without water intercalation in different electrolyte systems. Reproduced with permission.[72] Copyright 2018, Wiley-VCH.

strength will decrease accordingly. Choi's group studied the influence of structural water on Zn^{2+} ion diffusion paths and kinetic energy barriers in mixed-valent vanadium oxide, V_6O_{13}.[70] The nudged elastic band (NEB) calculation simulated possible Zn^{2+} ion diffusion pathways for the same distance, and the migration route along the *b*-axis possesses the lowest kinetic barrier for both cases. As illustrated in Figure 5c, Zn^{2+} ions prefer to migrate in a zigzag pattern from one octahedral site to the contiguous octahedral site within the water-intercalated V_6O_{13}, accompanied by water molecular rearrangement to impair electrostatic repulsion. For the water-free V_6O_{13} (Figure 5d), the diffusion of Zn^{2+} ions takes a straightforward route. The Zn^{2+} ion migration cross-sectional area analyses (Figure 5e) revealed that the water-intercalated V_6O_{13} had a higher Zn^{2+} ion insertion number, which can be ascribed to more freely Zn^{2+} ion migration in the water-enlarged diffusion channels. On a related note, the water-intercalated V_6O_{13}, as expected, showed a lower diffusion energy barrier than that of the water-free equivalent (0.87 vs 2.85 eV) (Figure 5f).

Typically, the structure of the guest ion hydration layer predominantly results from water coordination in the electrolyte. Through a controlled study where Wang et al. manipulated both the water content in the electrolyte and that within the V-based cathode material $VOPO_4$, it was demonstrated that water activity (α_{H2O}) governs the redistribution of water between $VOPO_4$ and the electrolyte until a dynamic H_2O equilibrium (Figure 5g) is attained.[71] As illustrated in Figure 5h, in a water-devoid electrolyte, $VOPO_4{\cdot}2H_2O$ showcases a vastly superior specific capacity (122 mAh g^{-1} vs ≈10 mAh g^{-1}) compared to $VOPO_4$.

To comprehend more about why and how the amount of intercalated water alters the V-based cathode in multiple aspects (i.e., interlayer spacing, electronic structure, charge density, Zn^{2+} ion diffusion, and electrostatic potential), Huang's group comprehensively discussed the effect of different water content on bilayer V_2O_5 through DFT investigations.[73] **Figure 6a** represents a typical V_2O_5 bilayer structure, which consists of layers perpendicular to the [001]-crystallographic direction and are stacked along the *c*-axis, held together by weak van der Waals interactions. As

© 2024 The Author(s). Advanced Energy Materials published by Wiley-VCH GmbH

16146840, 2024, 31, Downloaded from https://advanced.onlinelibrary.wiley.com/doi/10.1002/aenm.202401704 by University of Adelaide Alumni, Wiley Online Library on [02/04/2025]. See the Terms and Conditions (https://onlinelibrary.wiley.com/terms-and-conditions) on Wiley Online Library for rules of use; OA articles are governed by the applicable Creative Commons License

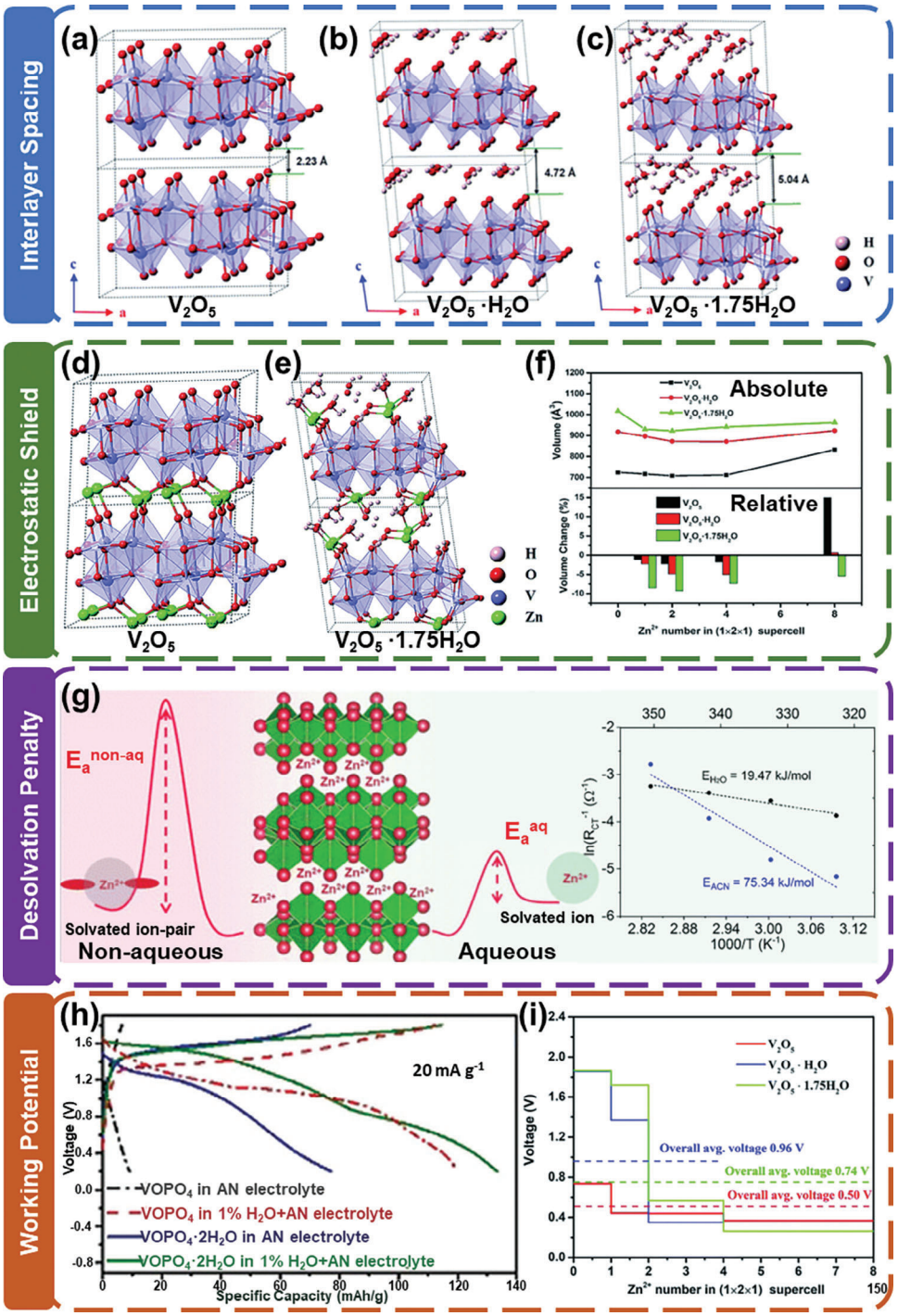


Figure 6. Impacts of water-intercalation on V-based cathode. The optimized supercells of bilayer interlayer V_2O_5 with different water content and corresponding calculated layer distance of a) V_2O_5, b) $V_2O_5{\cdot}H_2O$, and c) $V_2O_5{\cdot}1.75H_2O$. Structural configurations of 8 Zn^{2+} ions intercalated into d) V_2O_5 and e) $V_2O_5{\cdot}1.75H_2O$. f) The absolute (up) and relative (down) volumetric change for bilayer interlayer V_2O_5 with different water content after intercalating different numbers of Zn^{2+}. Reproduced with permission.[73a] Copyright 2019, The Royal Society of Chemistry. g) The schematic diagram of desolvation penalty at the interface with non-aqueous electrolyte and aqueous electrolyte for $V_3O_7{\cdot}H_2O$ and the difference of activation energy for interfacial charge transfer. Reproduced with permission.[71] Copyright 2018, The Royal Society of Chemistry. h) The GCD profiles of $VOPO_4$ and $VOPO_4{\cdot}H_2O$ with different working potential in 0.1 m $Zn(OTf)_2$-AN and 1%H_2O+0.1 m $Zn(OTf)_2$-AN electrolytes. Reproduced with permission.[72] Copyright 2018, Wiley-VCH. i) A comparison of the calculated average voltage for bilayer interlayer V_2O_5 based on varying water contents. Reproduced with permission.[73a] Copyright 2019, The Royal Society of Chemistry.

© 2024 The Author(s). Advanced Energy Materials published by Wiley-VCH GmbH

16146840, 2024, 31, Downloaded from https://advanced.onlinelibrary.wiley.com/doi/10.1002/aenm.202401704 by University of Adelaide Alumni, Wiley Online Library on [02/04/2025]. See the Terms and Conditions (https://onlinelibrary.wiley.com/terms-and-conditions) on Wiley Online Library for rules of use; OA articles are governed by the applicable Creative Commons License

compared in Figure 6b,c, the intercalated water can expand the interlayer spacing from 2.23 to 5.04 Å, when the crystalline water content increases from 1.0 to 1.75 per unit cell between the two V_2O_5 sheets. The final optimized structural configurations for 8 Zn^{2+} intercalated into the gallery of $V_2O_5{\cdot}1.75H_2O$ and V_2O_5 (Figure 6d,e) suggested that intercalation water can effectively shield the electrostatic interactions between Zn^{2+} and the neighbouring V_2O_5 sheets. During the process of Zn^{2+} intercalation from 0 to 8, all three vanadium cathodes exhibit an initial lattice contraction, followed by an expansion at elevated intercalation concentrations, which is driven by pronounced electrostatic interactions between the cations. Despite so, the cathodes with intercalated water have much less volume change than dry V_2O_5 (Figure 6f), suggesting improved structural stability for practical applications.

Hydration intercalation also plays a pivotal role in mitigating the energy losses associated with de-solvation at the electrode-electrolyte interface. In conventional rechargeable batteries, guest ions undergo desolvation at the interface. Owing to the heightened electrostatic interactions between guest ions and solvent molecules, the energy losses from the desolvation process of these guest ions are pronounced. However, the introduction of a hydration intercalation layer can reduce the desolvation energy, facilitating more efficient Zn^{2+} ion diffusion at the electrode-electrolyte juncture. For instance, Linda et al. reported there is an extra "desolvation penalty" in non-aqueous electrolytes than in aqueous ones for their $V_3O_7{\cdot}H_2O$ electrode.[71] The activation energy of the interfacial charge transfer resistance in the non-aqueous electrolytes is about four times larger than that in aqueous ones (Figure 6g).

Another notable advantage of intercalated water is that it can elevate the working voltage of V-based cathodes. For example, Wang et al. corroborated that crystalline H_2O in the $VOPO_4$ lattice can shift the Zn^{2+} insertion potential higher (Figure 6h),[72] opening an alternative way to tackle the low operational voltage issue. In Huang's work, the calculated average working voltage difference between dry V_2O_5 with $V_2O_5{\cdot}1.75H_2O$ is 0.46 V (Figure 6i).[73a] This excellent computational work undeniably uncovers the impacts of the intercalated water, providing significant insights for the modulation of V-based cathodes.

Lastly, some recent efforts include co-intercalated cation and water into V-based cathodes. Leveraging the use of the synergistic effect of cation plus structural water, this method is envisaged to provide superior performance. To date, a few combinations have been compiled by tweaking the cation species and the portion of water, such as $NH_4V_3O_8{\cdot}0.5H_2O$,[68b] $(NH_4)_2V_4O_9{\cdot}0.5H_2O$,[74] $NaCa_{0.6}V_6O_{16}{\cdot}3H_2O$,[75] $Mg_{0.34}V_2O_5{\cdot}0.84H_2O$,[76] $Zn_{0.34}V_2O_5{\cdot}0.37H_2O$,[77] and so on. Typically, Zheng's group synthesized hierarchically porous $Zn_{0.3}V_2O_5{\cdot}1.5H_2O$ (ZVO) nanoflowers via spontaneous phase transition from VOOH hollow nanospheres.[69] Benefiting from the intercalated zinc ions and water residing in interlayers which act as pillars and lubricants to stabilize the host structure, the ionic conductivity of material was promoted via electronic structure regulation. In consequence, the assembled battery delivers unparalleled cycle stability – more than 20000 cycles with a decent capacity of 214 mAh g^{-1} at 10 A g^{-1}.

In conclusion, water molecules exert a notably positive effect on the structure of electrode materials. First, they can expand the interlayer spacing, facilitating the intercalation of Zn^{2+} ions and enhancing the solid-state diffusion process. The extent of layer spacing expansion is closely linked to the quantity of water intercalated between the layers. Second, during the insertion of Zn^{2+} ions, these structured water molecules can act as a shield, mitigating the charge interaction between Zn^{2+} ions and the cathode matrix, thus reducing binding energy. Third, the incorporation of a small number of oxygen atoms (from water) into the material structure enhances its hydrophilicity, which contributes to the reduction of interface resistance, further improving the overall performance and efficiency of the battery system. Fourthly, structured water serves as an additional site for electron acceptance from Zn^{2+} ions, leading to stronger ionization and consequently increasing the open-circuit voltage (OCV) of the battery. The comprehensive effects of the intercalated water species are summarized in Figure 6.

3.1.6. Amorphization

For a lengthy period of time, crystalline materials were the predominant electrode materials in the battery field due to the fact that their regular atomic arrangement can provide unique space to accommodate embeddable ions. As their counterparts, the atomic cluster of amorphous materials are ordered in the short-range, whilst these clusters are linked in random in the long-range.[78] Ordinarily, many research works have considered the structural degradation or amorphization of electrode materials during charging and discharging as a principal cause of capacity degradation, given the collapse of the ordered structure might lead to the decay of ion storage sites.[79] However, intriguingly, some amorphous V-based cathode materials, such as $FeVO_4$,[80] V_2O_5,[81] VO_2,[82] etc., can be conducive to the full penetration of the electrolyte, accelerate Zn^{2+} ion diffusion by providing more isotropic diffusion routes and assist in releasing volume change strain during cycling.[83] These features render the amorphized materials unique advantages over their crystalline counterparts in terms of specific capacity and cycle stability. This segment will discuss these peculiar amorphous electrode materials and the provenance of their distinctive features in the following aspects: i) leveraging the utilization of active sites, ii) facilitating Zn^{2+} ion diffusion, iii) tolerating the concomitant volume changes.

The amorphous framework offers numerous exposed ionic channels, facilitating rapid charge transfer at the electrode/electrolyte interface. However, due to the generally poor conductivity of most V-based materials, they are typically blended with carbon additives during the preparation of cathodes. To further leverage its advantages and mitigate the drawback of poor conductivity, an innovative approach involves alternately stacking amorphous 2D nanosheets with types of highly conductive 2D nanosheets to form a 2D heterostructure. This configuration can generate strong synergistic effects, effectively merging the advantages of individual 2D nanosheets while simultaneously mitigating their respective drawbacks. For instance, Wu and co-workers developed an amorphous V_2O_5/graphene heterostructure (A-V_2O_5/G), combining different 2D nanosheets by stacking high-capacity V_2O_5 with highly conductive graphene to form a 2D nanosheet heterostructure, which outperformed the crystal V_2O_5 in terms of capacity and long-term cyclability.[84]

© 2024 The Author(s). Advanced Energy Materials published by Wiley-VCH GmbH

16146840, 2024, 31, Downloaded from https://advanced.onlinelibrary.wiley.com/doi/10.1002/aenm.202401704 by University of Adelaide Alumni, Wiley Online Library on [02/04/2025]. See the Terms and Conditions (https://onlinelibrary.wiley.com/terms-and-conditions) on Wiley Online Library for rules of use; OA articles are governed by the applicable Creative Commons License

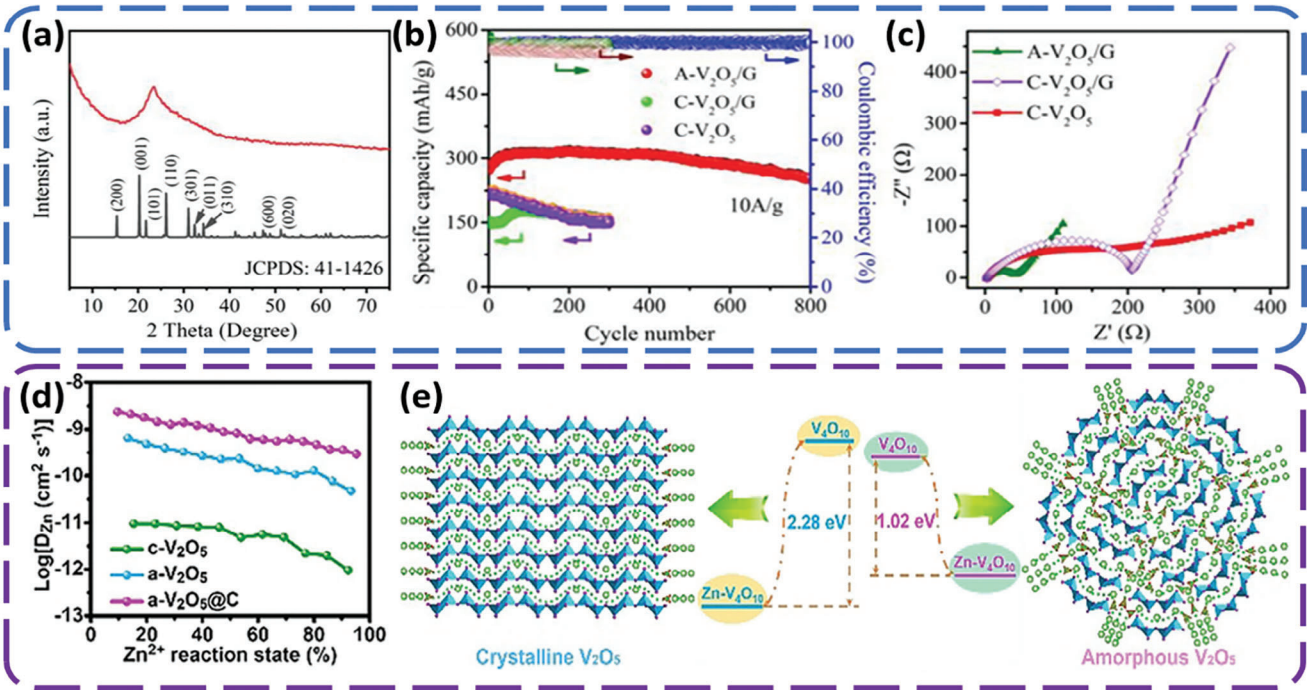


Figure 7. a) XRD patterns of amorphous V_2O_5/graphene heterostructure (A-V_2O_5/G) b) Cycling performance and c) electrochemical impedance spectra (EIS) of A-V_2O_5/G, crystalline V_2O_5/graphene heterostructure (C-V_2O_5/G), and pure crystalline V_2O_5. Reproduced with permission.[84] Copyright 2020, Wiley-VCH. d) The Zn^{2+} ion diffusion coefficient of crystalline V_2O_5 (c-V_2O_5), amorphous V_2O_5 (a-V_2O_5), and amorphous V_2O_5 and carbon composite (a-V_2O_5@C) during discharging e) Zn^{2+} ion (de)intercalation energy in crystalline and amorphous V_2O_5. Reproduced with permission.[85] Copyright 2020, Wiley-VCH.

XRD patterns (**Figure** 7a) of the A-V_2O_5/G with no diffraction peaks of standard V_2O_5 refer to its amorphous characteristics. In Figure 7b, the galvanostatic charge-discharge (GCD) profile shows poor cycle stability of the crystal cathode as its capacity drops sharply by 32% within 300 cycles. Against that, the amorphous V_2O_5/graphene heterostructure possesses a 27.2% higher capacity, while offering satisfactory capacity retention of ≈93% after 800 cycles. The author accredited this perceptible performance enhancement to the structural advantage of amorphism, which involves the nature of the disordered structural arrangement, resulting in a greater number of Zn^{2+} ion intercalation/deintercalation active sites and optimized kinetics. Moreover, due to the elimination of lattice constraints, the structure of amorphous V_2O_5 remains stable and can withstand volume fluctuation during cycling, resulting in greater cyclic stability than its crystalline counterpart. The electrochemical impedance spectra (EIS, Figure 7c) verified that the A-V_2O_5/G exemplified a lower charge transport resistance of 20 Ω, and lower voltage polarization of 0.64 V at the plateau region than that (102 Ω, 0.8 V) of crystal one.

Furthermore, the composite of amorphous electrode materials with carbon materials warrants attention. If the connection between V-based oxides and carbon materials is merely simple physical contact, as commonly seen in traditional cathodes, it would limit rapid electron transfer, leading to poor rate performance. To fundamentally address this challenge, Niu et al. reported a MOF-derived amorphous V_2O_5 (a-V_2O_5@C) with ultrahigh rate performances and a spectacular long-term cycle of 20000 cycles (91.4% capacity retention, 40 $A{\cdot}g^{-1}$).[85] The in situ electrochemical induction strategy triggers amorphization of V_2O_5 and enables more isotropic Zn^{2+} ion diffusion pathways and ion storage sites, culminating in impressive rate capability and specific energy capacity. The greatly heightened Zn^{2+} diffusion capability was also verified in diffusion coefficient measurements (Figure 7d) where the amorphous V_2O_5 exhibited a Zn^{2+} diffusion coefficient two orders of magnitude higher than the crystalline control sample. Additionally, the first-principal calculations (Figure 7e) revealed that the Zn^{2+} (de)intercalation energy in amorphous V_2O_5 is lower than the crystalline one (1.02 eV vs 2.28 eV, respectively), which represents an easier Zn^{2+} ion diffusion in amorphous V_2O_5.

In a nutshell, while generally considered to be detrimental, the amorphization of the V-based cathode materials in particular architectures/states can fully expose the otherwise less available active sites for Zn^{2+} intercalation. Direct advantages from amorphization include the enhanced overall reaction kinetic and specific capacity, together with a more open, isotropic framework for smaller lattice distortion and volume expansion under cycling. Despite many potential methods proposed for improvement, a major challenge with amorphous phase materials lies in the difficulty of determining their atomic structure and possible evolution during operation. Meanwhile, upon the amorphization treatment, one or several other types of defects (as those discussed above) can be concomitantly introduced. Hence, the structural changes during the energy storage process are challenging to be fully elucidated, making the precise mechanisms and sources of their energy storage contributions relatively vague. The lack of clarity hampers the rationales to optimize this type of

© 2024 The Author(s). Advanced Energy Materials published by Wiley-VCH GmbH

16146840, 2024, 31, Downloaded from https://advanced.onlinelibrary.wiley.com/doi/10.1002/aenm.202401704 by University of Adelaide Alumni, Wiley Online Library on [02/04/2025]. See the Terms and Conditions (https://onlinelibrary.wiley.com/terms-and-conditions) on Wiley Online Library for rules of use; OA articles are governed by the applicable Creative Commons License

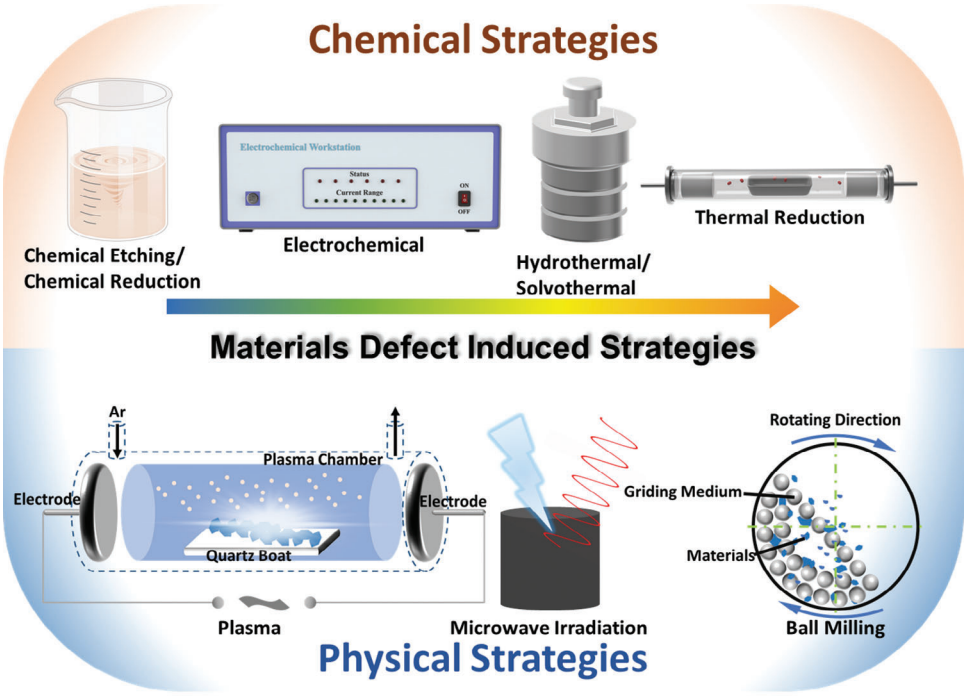


Figure 8. Schematic illustration of materials defect engineering strategies.

materials and/or to exploit their potential advantages in energy storage applications. Advanced characterization techniques and matched theoretical modelling are needed to gain a deeper understanding of the amorphous phase and its behaviors during energy storage, which is crucial for unlocking the full potential of these materials in practical applications.

3.1.7. Electrochemical Performances of Recent V-Based Cathodes with Defect Engineering

Defect engineering has made strides in the development of V-based cathode materials for AZIBs. To provide an intuitive understanding and benchmark study of impacts of various defect engineering strategies, we summarize the electrochemical performance of typical V-based cathode materials based on all these modification strategies reported in recent years. However, as demonstrated in the above discussion, defect engineering is inherently complex and multifaceted; many studies involve two or more strategies to achieve better electrochemical performance, yet authors usually highlighted one or two primary strategies as the key to the achieved performances. Therefore, typical results discussed in the above six sections are summarized in **Table 1**.

3.2. Materials Defect Induction Strategies

As discussed above, defects can affect the physical and chemical properties of a cathode. It is vital, therefore, to utilize effective synthesis methods to introduce these defects in a controllable manner. Given defects engineering has long been studied in many other materials for various applications, the corresponding techniques for defect fabrication are relatively mature. In general, techniques for engineering defects in V-based cathodes can be categorized into chemical and physical processes (**Figure 8**), with their specifics summarized as follows.

3.2.1. Chemical Strategies

The chemical strategies for defect preparation in materials can be broadly classified into four categories: thermal reduction, solvent chemical reduction, hydrothermal processes, and electrochemical methods. Regarding the thermal reduction method, high-temperature reduction can generate anionic vacancies on the surface. Actually, under an inert atmosphere, high-temperature annealing can provide activation energy that triggers the formation of defects, and by adjusting temperature, defect density can generally be controlled.[115] The following equation summarizes the relationship between structural defect concentration and temperature:

$$\frac{N_V}{N} = \exp\left(-\frac{Q_V}{k_B T}\right) \tag{6}$$

where N_V, N, Q_V, k_B, and T represent the number of defects in the lattice, activation energy for vacancy formation, Boltzmann's constant, and temperature, respectively. By adopting the high-temperature annealing method, Zhao et. al synthesized the defective $SNVO_X$-CNT (spherical NaV_6O_{15} cross-linked with carbon nanotubes) with rich V_Os under an Ar atmosphere at 450 °C.[116] In practice, high-temperature reductive hydrogen

© 2024 The Author(s). Advanced Energy Materials published by Wiley-VCH GmbH

16146840, 2024, 31, Downloaded from https://advanced.onlinelibrary.wiley.com/doi/10.1002/aenm.202401704 by University of Adelaide Alumni, Wiley Online Library on [02/04/2025]. See the Terms and Conditions (https://onlinelibrary.wiley.com/terms-and-conditions) on Wiley Online Library for rules of use; OA articles are governed by the applicable Creative Commons License

Table 1. Summary of the electrochemical performance comparison of Zn//V-based AZIBs.

Defect Type	Cathode material	Electrolyte	Voltage[V]	Specific capacity [mAh g^{-1}/A g^{-1}]	Energy density [Wh kg^{-1}]	Power density [kW kg^{-1}]	Cycle Performance [mA h g^{-1}/n/A g^{-1}]	Refs.
Oxygen Vacancy	V_6O_{13}	3 M $Zn(CH_3F_3SO_3)_2$	0.2–1.5	401/0.2	298	–	398/200/0.2	[33]
	O_d- $V_3O_7{\cdot}H_2O$@C	3 M $Zn(CH_3F_3SO_3)_2$	0.2–2.0	≈700/0.1	530	–	640/1000/5	[86]
	VO_2(B)	3 M $Zn(CF_3SO_3)_2$	0.3–1.5	375/0.1	–	–	175/2000/5	[32c]
	VO_2(B)	2 M $Zn(CF_3SO_3)_2$	0.2–1.4	355/0.1	–	–	150/700/3	[87]
	VO_2	4 M $Zn(CF_3SO_3)_2$	0.3–1.25	474/0.1	296	12	≈210/1000/10	[32a]
	$(NH_4)_2V_{10}O_{25}{\cdot}8H2O$	3 M $Zn(CF_3SO_3)_2$/PVA gel	0.4–1.5	408/0.1	287	5.7	160/4000/5	[36b]
	$K_2V_8O_{21}$	2 M $Zn(CF_3SO_3)_2$	0.1–1.7	385/0.2	272.6	–	258/1000/3	[38a]
	V_2O_5	3 M $Zn(CF_3SO_3)_2$	0.1–1.6	406/0.1	–	–	247/1000/2	[88]
	$NH_4V_3O_8$	3 M $Zn(CF_3SO_3)_2$	0.4–1.6	356.8/0.05	353.1	10	170.7/5000/10	[38b]
	$Na_{0.76}V_6O_{15}$	3 M $Zn(CF_3SO_3)_2$	0.3–1.5	256/0.1	228	3.16	165/2600/4	[35]
	$Cu_3V_2O_7(OH)_2{\cdot}2H_2O$	3 M $Zn(CF_3SO_3)_2$	0.4–1.6	286.5/0.2	–	–	115.2/3000/4	[89]
	$VO_2{\cdot}xH_2O$	2 M $ZnSO_4$	0.2–1.6	346.5/0.1	228	1.345	206/1000/10	[36d]
	ZVO	2 M $ZnSO_4{\cdot}7H_2O$	0.3–1.9	212.6/0.5	340.2	184.9	115.5/10 000/10	[90]
	$HNaV_6O_{16}{\cdot}4H_2O$ -Glu	3 M $Zn(CF_3SO_3)_2$	0.2–1.6	354.6/1	353	220	231.5/12 000/10	[91]
	VO-300	2 M $Zn(CF_3SO_3)_2$	0.3–1.6	544.96/0.1	–	–	411.98/1500/10	[92]
	V/O-defected NHVO	*3 M Zn $(CF_3SO_3)_2$*	*0.2–1.6*	*510/0.2*	–	–	*210/8000/15*	[93]
Cation Vacancy	D-VS_4	*3 M Zn $(CF_3SO_3)_2$*	0.1–1.8	300/0.2	–	–	1400/3500/10	[94]
	VS_2	1 M $ZnSO_4$	0.2–1.7	262/0.1	–	–	≈262/100/0.1	[95]
	V_2O_3	3 M $Zn(CF_3SO_3)_2$	0.2–1.6	328/0.8	340	46	≈225/800/3.2	[32b]
	$NH_4V_4O_{10}$	3 M $Zn(CF_3SO_3)_{22}$	0.1–1.6	357/1	317	0.392	280/1000/2	[42]
	Al-doped $V_{10}O_{24}{\cdot}12H_2O$	3 M $Zn(CF_3SO_3)_2$	0.4–1.6	415/0.2	–	–	294.5/3000/5	[57]
Cationic Doping	*(1 Zn, 1Ch)-VOH*	*3 M Zn$(CF_3SO_3)_2$*	*0.2–1.6*	*470/0.1*	*327*	*441*	*263/2000/4*	[96]
	3D NPG@S-NVO@CTAB	3 M $Zn(CF_3SO_3)_2$	0.2–1.6	525/0.5	381.2	525.8	356/2000/5	[97]
	Mn-VOH@GHC	*3 M Zn$(CF_3SO_3)_2$*	0.2–1.6	*530/0.2*	*491*	*273*	*344/2000/2*	[98]
	p-VON@C	*3 M Zn$(CF_3SO_3)_2$*	*0.2–1.8*	*518/1*	*180*	*275.5*	*296/2000/10*	[99]
	$Sn_{1.5}V_2O_7(OH)_2{\bullet}3.3H_2O$	1 M $ZnSO_4$	0.4–1.4	300/0.1	–	–	≈239.8/200/1	[56]
	$Ag_{0.4}V_2O_5$	3 M $ZnSO_4$	0.4–1.4	237/0.5	–	–	144/4000/20	[100]
	$Al_{0.2}V_2O_5$	3 M $Zn(CF_3SO_3)_2$	0.2–1.6	448.4/0.1	327.1	5.4918	84/5000/5	[101]
	$Zn_{0.25}V_2O_5{\cdot}nH_2O$	1 M $ZnSO_4$	0.5–1.4	≈300/0.5	250	–	≈250/1000/4.5	[49]
	$K_{0.5}V_2O_5$	3 M $Zn(CF_3SO_3)_2$	0.2–1.6	317/0.1	309	0.064	251/1000/5	[102]
	$Ru_{0.2}V_2O_5{\bullet}0.41H_2O$	2 M $Zn(CF_3SO_3)_2$	0.2–1.6	406/0.2	–	–	258/5000/10	[103]
	$Mg_{0.34}V_2O_5{\cdot}0.84H_2O$	3 M $Zn(CH_3F_3SO_3)_2$	0.1–1.8	353/0.05	–	–	≈60/2000/5	[76]
	$CaV_6O_{16}{\cdot}3H_2O$	4 M Zn $(CF_3SO_3)_2$	0.3–1.5	≈290/0.2	–	–	≈170/10 000/10	[104]
	$Zn_{0.3}V_2O_5{\cdot}1.5H_2O$	3 M 3 M $Zn(CF_3SO_3)_2$	0.3–1.6	426/0.2	268	1.4	214/20 000/10	[105]
	MnVO	3 M $Zn(CF_3SO_3)_2$	0.3–1.5	462.5/0.1	–	–	120/2500/5	[106]
	$Mn_{0.15}V_2O_5{\cdot}nH_2O$	1 M $Zn(ClO_4)_2$ in propylene carbonate	0.2–1.7	202/0.05	225	0.375	≈50/3000/2	[44]
	$Co_{0.247}V_2O_5{\cdot}0.944H_2O$	20 m LiTFSI + 1 m $Zn(TFSI)_2$	0.6–2.2	432/0.1	432	25.59	≈220(-)/7500/4	[63]
	$Al_{0.84}V_{12}O_{30.3}{\cdot}\ nH_2O$	3 M $Zn(CH_3F_3SO_3)_2$	0.2–1.6	380/0.5	257	6.3	221/3000/4	[107]
	$Na_{0.33}V_2O_5$	3 M $Zn(CH_3F_3SO_3)_2$	0.2–1.6	367.1/0.1	–	–	≈200(-)/1000/1	[51]
	$Ca_{0.25}V_2O_5{\cdot}n\ H_2O$	1 M $ZnSO_4$	0.6–1.6	340/0.2C	267	1.824	72/5000/80C	[108]
	$K_{0.5}V_2O_5\ {\cdot}0.76\,H_2O$	1 M $ZnSO_4$	0.4–1.4	421/0.5	341	121	≈156.3/1500/0.15	[109]
	$Na_3V_2(PO_4)_2F_3$	2 M $Zn(CF_3SO_3)_2$	0.8–1.9	60/0.2	95.4	4.4701	46/4000/1	[65a]
Anionic Doping	V_6O_{13}	3 M $Zn(CF_3SO_3)_2$	0.2–1.5	≈360/0.2	–	–	≈230/2000/4	[70]
Water Intercalation	*O_d-$V_2O_5{\cdot}4VO_2{\cdot}0.82\ H_2O$*	*3 M Zn$(CF_3SO_3)_2$*	*0.2–1.4*	*441.2/0.1*	–	–	*194.5/1000/20*	[110]
	$V_2O_5\ {\cdot}0.26H_2O$	3 M $ZnSO_4$	*0.3–1.6*	*370.2/0.5*	–	–	*327.5/2000/3*	[111]
	$NaV_3O_8{\cdot}1.5H_2O$	1 M $ZnSO_4$/1 M Na_2SO_4	0.3–1.25	380/0.05	300	3.6	≈100/1000/4	[58b]
	$V_2O_5{\cdot}n\ H_2O$	3 M $Zn(CH_3F_3SO_3)_2$	0.4–1.6	403.6/0.5	–	–	400/600/5	[112]

(*Continued*)

© 2024 The Author(s). Advanced Energy Materials published by Wiley-VCH GmbH

16146840, 2024, 31, Downloaded from https://advanced.onlinelibrary.wiley.com/doi/10.1002/aenm.202401704 by University of Adelaide Alumni, Wiley Online Library on [02/04/2025]. See the Terms and Conditions (https://onlinelibrary.wiley.com/terms-and-conditions) on Wiley Online Library for rules of use; OA articles are governed by the applicable Creative Commons License

Table 1. (Continued)

Defect Type	Cathode material	Electrolyte	Voltage[V]	Specific capacity [mAh g^{-1}/A g^{-1}]	Energy density [Wh kg^{-1}]	Power density [kW kg^{-1}]	Cycle Performance [mA h g^{-1}/n/A g^{-1}]	Refs.
	$NaCa_{0.6}V_6O_{16}{\cdot}3H_2O$	3 M $Zn(CH_3F_3SO_3)_2$	0.4–1.5	347/0.1	254	3.52	151/10 000/5	[75]
	$V_2O_5{\cdot}nH_2O$	3 M $Zn(CF_3SO_3)_2$	0.2–1.6	372/0.3	144	6.4	157/≈950/6	[68a]
	$(NH_4)_2V_4O_9{\cdot}0.5H_2O$	2 M $ZnSO_4$	0.3–1.3	338/0.2	309	9.324	177/1000/5	[74]
	$NH_4V_4O_{10}{\cdot}nH_2O$	3 M $Zn(CF_3SO_3)_2$	0.3–1.7	406/0.5	288	0.358	232/1500/10	[37]
	$NH_4V_3O_8{\cdot}0.5H_2O$	3 M $Zn(CF_3SO_3)_2$	0.3–1.3	423/0.1	353	0.114	≈300/1000/1	[68b]
	V_2O_5/graphene	3 M $ZnSO_4$ (V_2O_5 sol)	0.2–1.8	447/0.3	130	19.5	≈120/20 000/30	[81]
	V_2O_5@C	3 M $Zn(CF_3SO_3)_2$	0.3–1.9	620.2/0.3	–	–	≈272.6/20 000/40	[85]
Amorphization	2D V_2O_5/graphene	3 M $ZnSO_4$ (saturated by V_2O_5)	0.2–1.8	489/0.1	342	46	240/3000/30	[84]
	$VO_2{\cdot}0.5H_2O$	2 M $Zn(CH_3F_3SO_3)_2$	0.2–1.6	268/0.05	–	–	≈186/1000/1	[82]
	A-VO_xS_y	3 M $ZnSO_4$	0.2–1.8	535.8/0.1	234.75	7.5	237.8/20 000/40	[113]
	$FeVO_4$	1 M $Zn(ClO_4)_2$ in propylene carbonate	0.4–1.8	243/0.1	–	–	≈73.7/2500/5	[80]
	Amorphous polyaniline-coated/intercalated $V_2O_5{\cdot}nH_2O$	3 M $Zn(CF_3SO_3)_2$	0.3–1.6	444.3/0.1	–	–	157/1200/10	[114]

– represents the data are not available. Italic text indicates studies that involve the combined effects of two or more types of defects.

treatment, thermal treatment under other reactive (such as ammonia) atmospheres are more efficient in inducing V_O defects. High-valence vanadium oxides are one of the primary forms of V-based cathode materials. Partial reduction of the oxides can create defect structures, a key aspect in tailoring their electrochemical properties. During the high-temperature treatment, hydrogen gas reduces vanadium oxide to a lower valent state, altering the electronic structure and chemical properties of the surface layer (or even the whole bulk).[117] Taking the thermal reduction of V_2O_5 as an example, Xue et al. adopt $NaBH_4$ as the hydrogen source to generate V_Os in V_2O_5 at 400 °C for 1 h under the N_2 atmosphere.[88]

While the thermal reduction method is a popular and classical approach for introducing defects into materials, it is relatively cumbersome, energy-consuming, and requires specific temperatures and/or pressures. Comparatively, the use of reducing agents in solvent chemical reduction, such as $NaBH_4$ or N_2H_4, for the formation of defects presents obvious advantages like simple operations, uniform reactions, and mild reaction conditions. A pertinent example is that Luo et al. prepared V_O enriched VO_2 by $NaBH_4$ solution reduction at room temperature.[87] Apart from those two post-synthetic treatment methods, hydrothermal/solvothermal method can evenly create defects on materials' surfaces and/or bulk during the synthesis process. This method also enables more complex doping, such as cationic or anionic doping. For instance, using VCl_3, $Ca(NO_3)_2$, NaOH as V/Ca/Na source, Huang et al. prepared a Na/Ca co-doped $NaCa_{0.6}V_6O_{16}{\cdot}3H_2O$ barnesite nanobelts at 190 °C for 24 h with the hydrothermal method.[75] Lastly, electrochemical methods can effectively induce lattice distortions and generate a significant number of defects in materials. With this approach, various defects can be created during electrochemical cycling process driving by distinct electrical potentials, sometimes also termed as the activation process. Kim's group reported that the $VO_2{\cdot}0.5H_2O$ material experienced a crystalline-to-amorphous phase transformation under electrochemically oxidized at high voltages.[82] Similarly, Niu et al. adopt the in situ electrochemical oxidation method to convert V_2O_3 to V_2O_5 in the composite electrodes, where batteries were charged up to 1.9 V.[85]

In is worth mention that the listed examples are non-exhaustive for all these four chemical strategies; in fact, each method has the potential to create various types of defects. For instance, intercalation exfoliation using organic solvents or solvothermal methods that allow organic solvents and ions to penetrate the interlayers of nanosheets can also induce lattice distortions; chemical etching with strong acids or bases can create vacancy defects by dissolving more soluble metal components in the materials. Exploring chemical strategies that are more closely matched to the material and offer better cost-effectiveness remains a dynamic field.

3.2.2. Physical Strategies

In contrast to chemical strategies that are generally selective, physical strategies for engineering defects in V-based materials are relatively non-selective, though are still controllable to some extent. In literature, three physical strategies have been predominantly employed for defect engineering in V-based materials. First, plasma technology, which involves the application of ionized gases to modify material surfaces and induce defects. Second, microwave radiation, a technique that utilizes electromagnetic waves to induce structural changes within materials. Lastly, ball milling, a mechanical approach where materials are subject to grinding and blending processes, leading to the introduction of defects due to the high-energy impacts. Of these, plasma technology has become an effective tool for creating defects on the surfaces of materials in recent years. Plasma is the fourth state of matter and is composed of atoms, molecules, ions,

© 2024 The Author(s). Advanced Energy Materials published by Wiley-VCH GmbH

16146840, 2024, 31, Downloaded from https://advanced.onlinelibrary.wiley.com/doi/10.1002/aenm.202401704 by University of Adelaide Alumni, Wiley Online Library on [02/04/2025]. See the Terms and Conditions (https://onlinelibrary.wiley.com/terms-and-conditions) on Wiley Online Library for rules of use; OA articles are governed by the applicable Creative Commons License

and free radicals with equal amounts of positive and negative charges. Materials can be doped or defected quickly by the plasma technology without destroying their bulk structure or involvement in impurities. Today, plasmas are widely used for the synthesis and surface modification of materials because of their high electron temperatures, relatively low gas temperatures, and high energy characteristics. By generating spin within polar atoms through an electromagnetic field and converting that energy into thermal energy, microwave irradiation is a faster heating method compared to conventional heating. For example, Stefano et al. described an efficient method for preparing $CaV_6O_{16}\cdot 3H_2O$ cathode via microwave dielectric heating.[54] This approach can save 8 h each time compared to the previously reported hydrothermal method.[118] Zhou et al. utilized microwave technology to systematically prepare oxygen-deficient transition metal oxide materials with tuned electrical conductivity.[119] In their experiment, this method was shown to have a certain universality, since it could be used to prepare oxygen-deficient V_2O_5, WO_3, TiO_2, and Nb_2O_5. Microwave-assisted methods are believed to offer the advantages of scalability and improved response time, as well as a high potential for industrialization.

In addition to the aforementioned methods, ball milling is an attractive option for creating lattice distortions and defects. During ball milling, a ball and powder are enclosed in a closed container, subject to rotation and mechanical revolution, which generates kinetic energy and mechanical stress, leading to particle pulverization, lattice distortion, and structural imperfections. Despite so, for V-based oxides used in AZIB, physical methods remain relatively few for generating defects. It is yet to see whether further studies will be conducted into screening proper physical strategies for defect engineering in V-based cathodes.

4. Advanced Techniques on Defect Characterization and Theoretical Analysis

Defects in electrode materials are typically atomic-level, (sub)nanometer-sized, and with limited concentrations, all makes their quantification and qualitative characterization difficult with conventional methods.[120] Although defects disturb crystal lattices only slightly, they can have a profound impact on tuning the intrinsic characteristics. For example, enhance orbital hybridization and modify electron density near Fermi levels can produce more dangling bongs and unsaturated coordination sites. Particularly, the incorporation of defects into the crystal structure makes it possible to manipulate electrochemical properties.[121] In general, the most commonly used techniques for defect characterization can be distinguished as direct visualization techniques and indirect validation techniques. The high-resolution transmission electron microscope (HRTEM) used to be the most common direct visualization approach of defects, supplying the information of the type and density of defects. With the advancement of microscopic techniques, increasingly sophisticated electron microscopes, such as scanning transmission electron microscopy (STEM) and atomic-resolution scanning tunneling microscope (STM) were developed for direct observation of crystal defects. Alongside direct visualization, several technologies can be used to evaluate defects indirectly, such as X-ray photoelectron spectroscopy (XPS), electron paramagnetic resonance (EPR), positron annihilation spectroscopy (PAS), X-ray absorption spectroscopy (XAS) and so on. These characterization techniques are easy to use and widespread, but each has certain limitations are mostly exclusively for identification one specific defect types. Understanding how defects change their electronic structures requires always necessitate the application of theoretical calculations to reveal the mechanisms behind many phenomena and processes. One can, for instance, examine the DOS and energy band structure of pristine and defective materials to determine how the defects affect the conductivity of the materials. Additionally, since the ion conductivity is determined by the intercalation energy and the activation energy barrier of the diffusion pathways in the electrode material, theoretical calculations can simulate the different intercalation and diffusion pathways that may exist in the electrode material when a defect is present. In this session, we summarize the latest developments in characterization techniques and theoretical calculations for defect engineering.

4.1. Characterization Techniques

Direct visualization of defects usually relies on high-resolution microscopic techniques. The spatial resolution of traditional HRTEM is sufficient to discern distinguishable defects or large holes but reluctant in imaging vacancies. With the advancement of microscopy technologies, most prominently the application of aberration correction technology, the electron microscope has been capable of providing high-resolution images at low electron energies, facilitating the examination of a diversity of defect materials. Therein, the most often utilized approach is atomic-scale high-angle annular dark-field STEM (HAADF-STEM), which bypasses the complexities of diffraction contrast and coherent imaging and credits finer structural information. Chung et al. used atomic-column-resolved scanning transmission electron microscopy (STEM) with spherical aberration correction function to accurately observe the Zn and H_2O in the crystal lattice under the annular dark-field and annular bright-field (ABF) modes.[122] The atomic-resolution TEM images, shown in **Figure 9a**, allow direct visualization of the Zn and H_2O, which are consistent with the simulated images. Conversely to bright-field images, dark-field images tend to be more conducive to defect detection. These electron microscopes are capable of magnifying samples to the sub-nanometer or indeed atomic scale. STEM and energy dispersive spectroscopy (EDS) or electron energy loss spectroscopy (EELS) can be used in combination to further improve sub-angstrom element discrimination.

Compared to direct visualization methods, the indirect validation approach can provide a more comprehensive understanding of the internal defect. Herein, several prolific indirect validation techniques are outlined. Inchoate observations of defects often use XRD, XPS, and EPR. When specific defects are introduced into crystal structures, such as doping or amorphization, the periodic nature of the crystal structure is disturbed/destroyed. This can be detected by refined XRD. But generally, several other type of defects cannot be well observed from XRD, thus this method was applied as an auxiliary approach to observe the defect influence on the crystal structure upon battery cycling. Wang et al. reported that, due to the low doping level, the XRD

© 2024 The Author(s). Advanced Energy Materials published by Wiley-VCH GmbH

16146840, 2024, 31, Downloaded from https://advanced.onlinelibrary.wiley.com/doi/10.1002/aenm.202401704 by University of Adelaide Alumni, Wiley Online Library on [02/04/2025]. See the Terms and Conditions (https://onlinelibrary.wiley.com/terms-and-conditions) on Wiley Online Library for rules of use; OA articles are governed by the applicable Creative Commons License

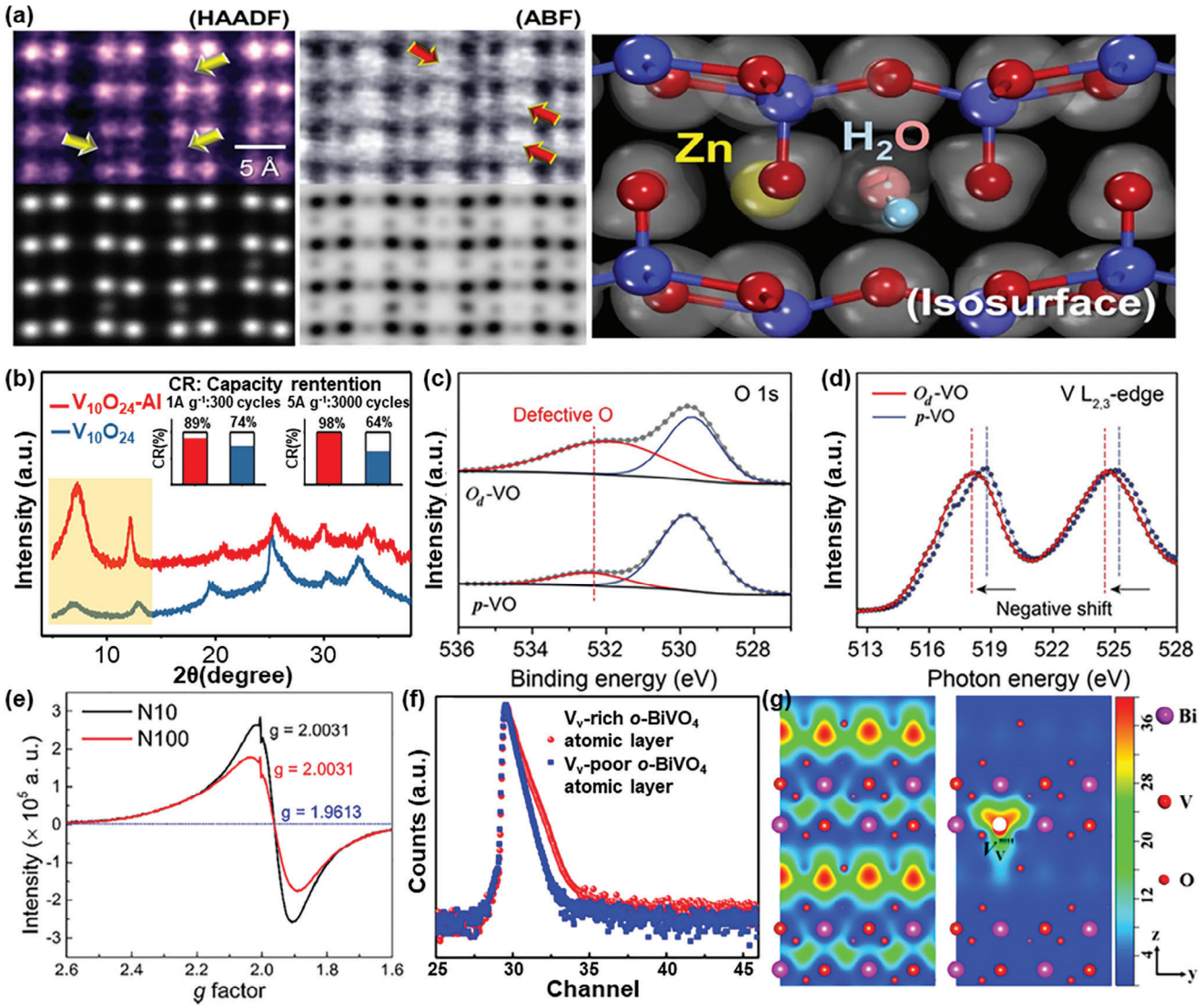


Figure 9. a) Atomic-scale HAADF-STEM and ABF-STEM images of $Zn_yV_2O_5{\cdot}nH_2O$. The yellow and red arrows point out the Zn and inserted H_2O in the crystal lattice, respectively. Reproduced with permission.[122] Copyright 2021, Springer Nature. b) XRD patterns of $V_{10}O_{24}$ and Al-doped $V_{10}O_{24}$ electrodes after long-term cycling. Reproduced with permission.[57] Copyright 2019, American Chemical Society. c) O 1s XPS spectra and d) V $L_{2,3}$-edge XANES spectra of pristine-V_6O_{13} (*p*-VO) and oxygen-deficient-V_6O_{13} (O_d-VO). Reproduced with permission.[33] Copyright 2019, Wiley-VCH. e) EPR profiles of $NH_4V_4O_{10}{\cdot}x{\cdot}nH_2O$ with different amounts of oxygen vacancies. Reproduced with permission.[123] Copyright 2021, Springer Nature. f) PALS spectra and g) Trapped positrons schematic for V_v-rich and V_v-poor *o*-$BiVO_4$. Reproduced with permission.[125] Copyright 2017, American Chemical Society.

pattern cannot discern obvious peak position shifts in terms of the Al-doped $V_{10}O_{24}$ and Al-free one.[57] However, the XRD results of the sample which experienced long-term cycling appearance are much different according to Figure 9b. After long-term cycling, the signal peaks of $V_{10}O_{24}$ become board and attenuated, which represents the structure destruction by Zn^{2+} ion insertion/extraction. On the contrary, Al-doped $V_{10}O_{24}$ shows good crystallinity which supports the conclusion that the doping of Al can benefit the cycling stability.

XPS is a quantitative surface-sensitive technique that provides information (i.e., elemental composition, chemical valence states, electronic states) of the elements. In practice, XPS has been usually used for characterizing vacancies by combining with X-ray absorption near-edge spectroscopy (XANES). Extended XANES is to analyze the chemical environment around the material atoms by using the fluorescence of photoelectrons emitted from the sample after X-rays are irradiated. The phenomenon of extended X-ray absorption is determined by the short-range ordering effect. From the structure spectrum, the type, distance, coordination number and other data of the adjacent coordination atom of the absorption atom can be obtained. The content of defects can be obtained qualitatively by observing the deviation of the distance between adjacent coordinating atoms and the intensity of the peak. In Peng's work, partial oxygen-extracted V_6O_{13} samples were studied with XPS and XANES.[33] The XPS spectrum (Figure 9c) shows that the hydroxy groups (V−OH) peak intensity was increased after the introduction of Vo. Meanwhile, the V $L_{2,3}$-edge XANES results (Figure 9d)

© 2024 The Author(s). Advanced Energy Materials published by Wiley-VCH GmbH

16146840, 2024, 31, Downloaded from https://advanced.onlinelibrary.wiley.com/doi/10.1002/aenm.202401704 by University of Adelaide Alumni, Wiley Online Library on [02/04/2025]. See the Terms and Conditions (https://onlinelibrary.wiley.com/terms-and-conditions) on Wiley Online Library for rules of use; OA articles are governed by the applicable Creative Commons License

exhibit a negative shift which represents the decrease of V valence caused by oxygen extraction.

EPR, also known as electron spin resonance (ESR), is another powerful and non-destructive method to study materials with unpaired electrons based on the fact that every electron possesses a magnetic moment and a spin quantum number ($m_s = \pm 1/2$). Wang et al. investigated $NH_4V_4O_{10}$·x·nH_2O materials containing oxygen defects with EPR.[123] By controlling the hydrothermal time at the same temperature, materials with different degrees of oxygen defects were obtained and their structures were characterized. EPR analysis (Figure 9e) showed that the materials prepared with different hydrothermal times all contain a certain amount of oxygen defects, corresponding to the first derivative peak at $g \approx 2.0031$. In addition, with the extension of the hydrothermal time, the oxygen defect peak gradually became stronger and wider, which proves that the concentration of defects in the material gradually increased.

Like EPR, positron annihilation spectroscopy (PALS) is another non-destructive, powerful technique that studies the interior chemical information of bulk samples. This technique is widely used to detect the presence of defects and vacancies in solid materials. The principle of PALS is to detect the annihilation information when the positron interacts with the electron, during which the relaxation time of the gamma rays released can be recorded.[124] The length of the relaxation time depends on the size of the vacancies/pores (can be atomic scale) of the material. The PALS test usually gives out three positron lifetime components: τ_1, τ_2, and τ_3. The first component τ_1 represents the free annihilation of positrons. Another two longer life components τ_2 and τ_3 refer to the existence of large voids and the interface under the samples. As an example, Wang et al. investigated the types and quantities of V_V of the synthesized $BiVO_4$ sample using PALS (Figure 9f,g).[125] τ_1 is the shortest lifetime component was attributed to V_V trapped positron annihilation. τ_1 for V_v-poor *o*-$BiVO_4$ atomic layer was 200.1 ± 20 ps, whereas τ_1 for V_v-rich *o*-$BiVO_4$ atomic layer was extended to 208.9 ± 18 ps. It was suggested that the defects in the crystal system can decrease the electron density, and the lower electron density around large-size defects can reduce the annihilation rate and increase the lifetime of positrons.[87] Besides proving the existence of V_V, PALS also supplies information about the concentration of vacancy.

4.2. Theoretical Calculations

Theoretical calculations are powerful in interpreting the structure-performance relationship of materials by providing atomic-level insights. To deeply understand the mechanism of defect engineering-induced effects in V-based cathode materials' capacity, rate performance, and cycle stability, substantial theoretical research has been carried out either independently or in combination with experimental measurements. In most existing literatures, theoretic calculations provide the information including the DOS changes of the materials, Zn^{2+} adsorption energies of active sites, intercalation energies, diffusion energy barries of the defect-modified V-based materials. For instance, Li et al. calculated the adsorption energies of Zn^{2+} ions on the surface of VSe_2 and Se-deficient VSe_2.[126] They reported the Se-deficient sample showed thermally neutral adsorption energy, representing reversible Zn^{2+} ion adsorption/desorption. The authors also correlated this with the effective utilization of active sites and a significant improvement in the cycle performance of the material. Similarly, Wang et al. observed that the introduction of V_O into the V_2O_5@CC could lead to the ΔG_{Zn2+} increase from −1.29 to −0.18 eV.[127] Besides the promoted cycling performance, the oxygen-deficient V_2O_5@CC showed improved capacity, which was explained by simulating the charge state difference of the samples with/without defects. Generally, the electron cloud in a perfect material is evenly distributed. The introduction of defects will break the even distribution and cause electron clouds to accumulate on the surface of the defective sites. Wang's simulation results confirmed this, where the defect causes the generation of spare electrons that could contribute to the delocalized electron cloud of oxygen-deficient V_2O_5@CC, thus leading to a capacity improvement.[127] The intercalation and diffusion of Zn^{2+} ions are critical processes in the study of V-based cathodes for AZIB. Even with the same structure, there are many site possibilities for intercalation and many pathways for diffusion. To find the most probable ones, it is typically necessary to calculate and analyze the energy barriers for diffusion activation at each site and pathway. Cao et al. calculate the activation barriers of Zn^{2+} ion diffusion via NEB calculations using the Ab initio Simulation Package (VASP).[32c] It shows that the migration energy barrier can be decreased with the introduction of V_O (from 0.71 to 0.24 eV). Similarly to the trapping state, when Zn^{2+} ion passes through the V_O, it will be trapped in this site and remain in a metastable state.[128]

5. Summary and Outlook

In this comprehensive review, we have delved into the intricate roles of defect engineering in augmenting the electrochemical performances of V-based cathode materials for AZIBs. V-based cathodes, pivotal in the realm of AZIBs, present a broad redox range and compatibility with water's electrochemical constraints. However, despite their potential and advantages, these cathodes face critical challenges impeding their transition from laboratory breakthroughs to commercial reality. These challenges encompass structural degradation, low operating voltage, and active material dissolution under aqueous conditions, all of which culminate in limiting the long-term stability and energy density of the assembled batteries. The central thrust of this review has been the exploration and systematic understanding of defect engineering as a transformative technique to fine-tune the electronic properties of V-based cathodes. This approach harnesses a variety of defects, including Vo_S, cation vacancies, cationic and anionic doping, water intercalation, and lattice disorder/amorphization, to enhance Zn^{2+} ion kinetics and electronic conductivity. These modifications have also shown markedly potential to improve the structural stability of electrodes, contribute to augmented discharge capacities, and overall elevate electrochemical performance.

Special emphasis has been placed on the strategic introduction and control of V_Os. This type of vacancy has been the most commonly critical agent in optimizing Zn^{2+} ion diffusion and amplifying the ionic conductivity of the cathodes. Similarly, the incorporation of cation vacancies and diverse doping strategies

© 2024 The Author(s). Advanced Energy Materials published by Wiley-VCH GmbH

16146840, 2024, 31, Downloaded from https://advanced.onlinelibrary.wiley.com/doi/10.1002/aenm.202401704 by University of Adelaide Alumni, Wiley Online Library on [02/04/2025]. See the Terms and Conditions (https://onlinelibrary.wiley.com/terms-and-conditions) on Wiley Online Library for rules of use; OA articles are governed by the applicable Creative Commons License

has demonstrated significant potential in addressing the intrinsic limitations like slow ion diffusion and low electrode stability. A particularly intriguing aspect covered in this review is the discussion of the intercalated water molecules within the electrode structure, which are elucidated as a novel strategy to expand layer spacing, facilitate ion intercalation, elevate operation voltage, stabilize cathode structures, and enhance overall electrochemical efficiency. The intriguing amorphization strategy was also highlighted, which have been recognized for their potential to offer more isotropic diffusion routes and accommodate volume changes during cycling. This confers them unique advantages in terms of specific capacity and cycle stability over their crystalline counterparts. However, a major hurdle in leveraging these amorphous materials lies in the difficulty of determining their precise atomic structure and comprehensively deciphering their energy storage mechanisms. The fabrication methods and advanced characterization techniques of defective electrode materials from recent reports have also been summarized. A benchmarking study of electrochemical performance of the V-based electrodes modified using all the six defect engineering strategies are also listed.

Looking ahead, the field beckons for further research dedicated to refining defect engineering strategies. This includes an emphasis on managing defect concentrations and types more effectively and precisely, to optimize material performance. Concurrently, there is a pressing need for advances in characterization techniques and theoretical modelling, to unravel the intricate behaviors of these defects during energy storage processes. Moreover, the development of environmentally benign and cost-effective synthesis methods remains paramount. In order to further promote the application of defective V-based electrodes, some specific perspectives are listed as follows:

1) *Emphasizing the role of water*: The electrolyte acts like blood in the AZIBs, providing a pathway for Zn^{2+} ions to transverse between the cathode and anode. However, free water in the electrolyte is a primary factor leading to the irreversible dissolution of V-based materials. Strategies such as adding additives, adjusting electrolyte concentration with a "water-in-salt" approach, incorporating organic co-solvents, or introducing gel electrolytes can be effective solutions. It's important to balance the decreased ionic conductivity that may result from these adjustments. Another aspect of water to consider is the structural water in V-based cathode materials. Often overlooked, structural water is a common defect that has unique advantages. Proper amount of structural water can mitigate charge repulsion effects through electrostatic shielding. Furthermore, water molecules in the material often lead to changes in the crystal structure, typically resulting in expanded layer spacing and acting as a pillar to stabilize the framework. Controlling the content of structural water during electrode material preparation is essential for optimizing performance.
2) *Dynamics and annihilation of defects*: Special attentions should be paid to the dynamic evolution and annihilation of defects, for instance cation vacancies which are initially carrier storage sites and the inserted ion may be difficult to detach. It is important to observe how different defects will evolve during initial cycles and change after long-term cycling. Assess whether defects still exist and if their concentration changes significantly. In the V-based system, especially under mildly acidic aqueous conditions, issues like dissolution, byproduct formation, phase transformation, and the dynamic evolution of defects need careful examination.
3) *Scalable and controllable defect engineering protocols*: Despite defects' intriguing properties in modifying V-cathodes, their scalable fabrication method has been limited. Existing literature usually deploy single method to fabrication certain type of defect. Ensuring the reproducibility and reliability of large-scale synthesis of defective materials is critical for commercial development. The process should be designed to consistently produce the desired types and concentrations of defects.
4) *Impacts of defects in microstructures of materials*: Many microstructures of electrode materials play essential roles in regulating their electrochemical performances. For instance, The V-based materials with different exposed facets have different atomic rearrangement and coordination configurations, hence exhibiting different electronic structures (bandgap, band edge potential, etc.), electrical conductivity, surface built-in electric field. In LIBs, specific exposed facets have been evidenced to foster an accelerated guest ion insertion/desorption process, often realizing nearly 100% of the theoretical capacity through favored pathways. While the prominence of facet-dependent behaviors is well-established in several cathode materials due to its intimate connection with guest ion diffusion pathways, its study on the zinc-ion aqueous battery systems, especially with V-based cathode materials, remains relatively shallow.[87,129]
5) *Interactive Effects of Multiple Defects*: Investigate whether the presence of two or more defects always results in a synergistic or antagonistic influence on the material's performance. This aspect is crucial for understanding the complex interactions between different types of defects and their collective impact on electrochemical properties. For example, in situ amorphization could occur during battery cycling, leading to transformations in defect types and/or the co-introduction of other defect types. This dynamic or multi-stage evolution of material defects is an area that deserves closer attention in future studies.
6) *Are all defects beneficial?* The idealization that defects invariably lead to positive outcomes oversimplifies their complex nature. Defects can indeed improve ionic conductivity and structural stability; however, if not properly controlled, they can also introduce unfavorable electronic states, reduce charge carrier mobility, and/or destabilize the crystal structure. Excessive defect density, in particular, may lead to structural weaknesses and accelerated degradation under operational stresses. To harness the benefits of defects without incurring these drawbacks, future research should prioritize a strategic approach to defect engineering. This includes selecting the appropriate types of defects and controlling their concentration within the cathode material. Advanced modelling and simulation, coupled with rigorous experimental validation, are essential to achieve a deeper understanding of defect interactions.
7) *Developing advanced modelling methods*: There are various types of defects, and their specific characteristics are also diverse. Using the traditional trial-and-error method to screen

© 2024 The Author(s). Advanced Energy Materials published by Wiley-VCH GmbH

16146840, 2024, 31, Downloaded from https://advanced.onlinelibrary.wiley.com/doi/10.1002/aenm.202401704 by University of Adelaide Alumni, Wiley Online Library on [02/04/2025]. See the Terms and Conditions (https://onlinelibrary.wiley.com/terms-and-conditions) on Wiley Online Library for rules of use; OA articles are governed by the applicable Creative Commons License

efficient defect engineering methods is extremely slow and impractical. Emerging simulation methods, such as machine learning and high-throughput screening, can greatly accelerate the traditional screening process and deepen the understanding of structure-performance inter-relationship between defects and material, thereby efficiently guiding material synthesis and saving costs. Research in this area, just like in other fields, deserves special attention.

Acknowledgements

The authors thank for financial support from the Australian Research Council Discovery Early Career Researcher Award (DE200101669). Z.P. thanks for the University of Sydney Horizon Fellowship scheme. X.Z. thanks for the support from the China Scholarship Council (CSC), the Ministry of Education of China.

Open access publishing facilitated by The University of Sydney, as part of the Wiley - The University of Sydney agreement via the Council of Australian University Librarians.

Conflict of Interest

The authors declare no conflict of interest.

Keywords

defect engineering, energy storage, vanadium cathodes, zinc-ion batteries

Received: April 16, 2024
Revised: May 19, 2024
Published online: June 4, 2024

[1] a) M. Tran, D. Banister, J. D. Bishop, M. D. McCulloch, *Nat. Clim. Change* **2012**, *2*, 328; b) J. J. Ye, P. H. Li, H. R. Zhang, Z. Y. Song, T. Fan, W. Zhang, J. Tian, T. Huang, Y. Qian, Z. Hou, N. Shpigel, L. Chen, S. Dou, *Adv. Funct. Mater.* **2023**, *33*, 2305659.

[2] T. C. Wanger, *Conserv. Lett.* **2011**, *4*, 202.

[3] a) E. C. Evarts, *Nature* **2015**, *526*, S93; b) S. Chen, C. Wu, L. Shen, C. Zhu, Y. Huang, K. Xi, J. Maier, Y. Yu, *Adv. Mater.* **2017**, *29*, 1700431; c) J. C. Pramudita, D. Sehrawat, D. Goonetilleke, N. Sharma, *Adv. Energy Mater.* **2017**, *7*, 1602911; d) S. Xu, Y. Yang, F. Tang, Y. Yao, X. Lv, L. Liu, C. Xu, Y. Feng, X. Rui, Y. Yu, *Mater. Horiz.* **2023**, *10*, 1901.

[4] a) J. Ni, S. Fu, C. Wu, J. Maier, Y. Yu, L. Li, *Adv. Mater.* **2016**, *28*, 2259; b) A. Ponrouch, C. Frontera, F. Bardé, M. R. Palacín, *Nat. Mater.* **2016**, *15*, 169; c) G. Fang, J. Zhou, A. Pan, S. Liang, *ACS Energy Lett.* **2018**, *3*, 2480; d) A. Ponrouch, J. Bitenc, R. Dominko, N. Lindahl, P. Johansson, M. R. Palacín, *Energy Storage Mater.* **2019**, *20*, 253; e) Y. Liang, H. Dong, D. Aurbach, Y. Yao, *Nat. Energy* **2020**, *5*, 646; f) Z. Chen, T. Wang, Y. Hou, Y. Wang, Z. Huang, H. Cui, J. Fan, Z. Pei, C. Zhi, *Adv. Mater.* **2022**, *34*, 2207682.

[5] a) C. Wang, X. Zeng, P. Cullen, Z. Pei, *J. Mater. Chem. A* **2021**, *9*, 19054; b) C. Wang, X. Zeng, J. Qu, J. M. Cairney, Q. Meng, P. J. Cullen, Z. Pei, *Matter* **2023**, *6*, 3993.

[6] a) D. Wang, Q. Li, Y. Zhao, H. Hong, H. Li, Z. Huang, G. Liang, Q. Yang, C. Zhi, *Adv. Energy Mater.* **2022**, *12*, 2102707; b) Z. Pei, L. Ding, C. Wang, Q. Meng, Z. Yuan, Z. Zhou, S. Zhao, Y. Chen, *Energy Environ. Sci.* **2021**, *14*, 4926; c) Z. Pei, Z. Yuan, C. Wang, S. Zhao, J. Fei, L. Wei, J. Chen, C. Wang, R. Qi, Z. Liu, Y. Chen, *Angew. Chem., Int. Ed.* **2020**, *59*, 4793.

[7] a) G. Fang, C. Zhu, M. Chen, J. Zhou, B. Tang, X. Cao, X. Zheng, A. Pan, S. Liang, *Adv. Funct. Mater.* **2019**, *29*, 1808375; b) Y. Cai, F. Liu, Z. Luo, G. Fang, J. Zhou, A. Pan, S. Liang, *Energy Storage Mater.* **2018**, *13*, 168; c) L. Ma, S. Chen, C. Long, X. Li, Y. Zhao, Z. Liu, Z. Huang, B. Dong, J. A. Zapien, C. Zhi, *Adv. Energy Mater.* **2019**, *9*, 1902446; d) Q. Zhao, W. Huang, Z. Luo, L. Liu, Y. Lu, Y. Li, L. Li, J. Hu, H. Ma, J. Chen, *Sci. Adv.* **2018**, *4*, aao1761; e) H. Glatz, E. Lizundia, F. Pacifico, D. Kundu, *ACS Appl. Energy Mater.* **2019**, *2*, 1288.

[8] a) G. Li, L. Sun, S. Zhang, C. Zhang, H. Jin, K. Davey, G. Liang, S. Liu, J. Mao, Z. Guo, *Adv. Funct. Mater.* **2024**, *34*, 2301291; b) Y. Bai, Y. Qin, J. Hao, H. Zhang, C. M. Li, *Adv. Funct. Mater.* **2024**, *34*, 2310393.

[9] N. Ortiz-Vitoriano, N. E. Drewett, E. Gonzalo, T. Rojo, *Energy Environ. Sci.* **2017**, *10*, 1051.

[10] L. Chen, Q. An, L. Mai, *Adv. Mater. Interfaces* **2019**, *6*, 1900387.

[11] S. Liu, L. Kang, J. M. Kim, Y. T. Chun, J. Zhang, S. C. Jun, *Adv. Energy Mater.* **2020**, *10*, 2000477.

[12] a) J. Wu, Q. Kuang, K. Zhang, J. Feng, C. Huang, J. Li, Q. Fan, Y. Dong, Y. Zhao, *Energy Storage Mater.* **2021**, *41*, 297; b) P. Y. Zavalij, M. S. Whittingham, *Acta Crystallogr., Sect. B: Struct. Sci.* **1999**, *55*, 627; c) X. Zhang, Z. Zhang, S. Xu, C. Xu, X. Rui, *Adv. Funct. Mater.* **2023**, *33*, 2306055.

[13] a) M. Wu, C. Shi, J. Yang, Y. Zong, Y. Chen, Z. Ren, Y. Zhao, Z. Li, W. Zhang, L. Wang, X. Huang, W. Wen, X. Li, X. Ning, X. Ren, D. Zhu, *Adv. Mater.* **2024**, *36*, 2310434; b) J. Wu, Z. Yang, H. Chen, L. Deng, Y. Rong, Z. Fu, *Appl. Surf. Sci.* **2022**, *592*, 153137; c) L. Liu, T. Yuan, Z. Li, K. Chen, W. Huang, *Electrochim. Acta* **2023**, *439*, 141717.

[14] R. Wang, X. Chen, Z. Huang, J. Yang, F. Liu, M. Chu, T. Liu, C. Wang, W. Zhu, S. Li, *Nat. Commun.* **2021**, *12*, 3085.

[15] a) Y. Zhang, L. Tao, C. Xie, D. Wang, Y. Zou, R. Chen, Y. Wang, C. Jia, S. Wang, *Adv. Mater.* **2020**, *32*, 1905923; b) X. Wang, Z. Zhang, B. Xi, W. Chen, Y. Jia, J. Feng, S. Xiong, *ACS Nano* **2021**, *15*, 9244; c) K. Zhu, S. Wei, H. Shou, F. Shen, S. Chen, P. Zhang, C. Wang, Y. Cao, X. Guo, M. Luo, H. Zhang, B. Ye, X. Wu, L. He, L. Song, *Nat. Commun.* **2021**, *12*, 6878; d) X. Huo, L. Xu, K. Xie, K. Zhang, J. Li, D. Wang, K. Shu, *Adv. Energy Mater.* **2023**, *13*, 2203066.

[16] X. Zhang, D. Li, Q. Ruan, L. Liu, B. Wang, F. Xiong, C. Huang, P. K. Chu, *Mater. Today Energy* **2022**, *32*, 101232.

[17] X. Xu, F. Xiong, J. Meng, X. Wang, C. Niu, Q. An, L. Mai, *Adv. Funct. Mater.* **2020**, *30*, 1904398.

[18] F. Lanlan, L. Zhenhuan, D. Nanping, *Energy Storage Mater.* **2021**, *41*, 152.

[19] F. Wan, Z. Niu, *Angew. Chem.* **2019**, *131*, 16508.

[20] C. Liu, R. Massé, X. Nan, G. Cao, *Energy Storage Mater.* **2016**, *4*, 15.

[21] a) Z. Wu, C. Lu, Y. Wang, L. Zhang, L. Jiang, W. Tian, C. Cai, Q. Gu, Z. Sun, L. Hu, *Small* **2020**, *16*, 2000698; b) P. He, M. Yan, G. Zhang, R. Sun, L. Chen, Q. An, L. Mai, *Adv. Energy Mater.* **2017**, *7*, 1601920; c) Y. Bai, L. Luo, W. Song, S. Man, H. Zhang, C. M. Li, *Adv. Sci.* **2024**, *11*, 2308668.

[22] J. Ding, H. Gao, D. Ji, K. Zhao, S. Wang, F. Cheng, *J. Mater. Chem. A* **2021**, *9*, 5258.

[23] a) H. Li, J. Li, Z. Ai, F. Jia, L. Zhang, *Angew. Chem., Int. Ed.* **2018**, *57*, 122; b) H. Jiang, J. Gu, X. Zheng, M. Liu, X. Qiu, L. Wang, W. Li, Z. Chen, X. Ji, J. Li, *Energy Environ. Sci.* **2019**, *12*, 322; c) Y. Gong, J. Zhang, L. Jiang, J.-A. Shi, Q. Zhang, Z. Yang, D. Zou, J. Wang, X. Yu, R. Xiao, *J. Am. Chem. Soc.* **2017**, *139*, 4274; d) R. Chattot, O. L.e Bacq, V. Beermann, S. Kühl, J. Herranz, S. Henning, L. Kühn, T. Asset, L. Guétaz, G. Renou, *Nat. Mater.* **2018**, *17*, 827.

[24] a) W. Zhong, Z. Shen, J. Mao, S. Zhang, H. Cheng, Y. Kim, Y. Lu, *Energy Environ. Sci.* **2024**, *17*, 2059; b) Y. Zou, X. Yang, L. Shen, Y. Su, Z. Chen, X. Gao, J. Zhou, J. Sun, *Energy Environ. Sci.* **2022**, *15*, 5017; c) Y. Dai, C. Zhang, J. Li, X. Gao, P. Hu, C. Ye, H. He, J. Zhu, W. Zhang, R. Chen, *Adv. Mater.* **2024**, *36*, 2310645; d) Y. Kim, Y. Park, M. Kim, J. Lee, K. J. Kim, J. W. Choi, *Nat. Commun.* **2022**, *13*, 2371.

© 2024 The Author(s). Advanced Energy Materials published by Wiley-VCH GmbH

16146840, 2024, 31, Downloaded from https://advanced.onlinelibrary.wiley.com/doi/10.1002/aenm.202401704 by University of Adelaide Alumni, Wiley Online Library on [02/04/2025]. See the Terms and Conditions (https://onlinelibrary.wiley.com/terms-and-conditions) on Wiley Online Library for rules of use; OA articles are governed by the applicable Creative Commons License

[25] a) S. Boyd, V. Augustyn, *Inorg. Chem. Front.* **2018**, *5*, 999; b) Y. Lu, T. Zhu, W. van den Bergh, M. Stefik, K. Huang, *Angew. Chem.* **2020**, *132*, 17152.
[26] Z. Xing, G. Xu, J. Han, G. Chen, B. Lu, S. Liang, J. Zhou, *Trends Chem.* **2023**, *5*, 380.
[27] K. Illeris, *Contemporary Theories of Learning*, 2nd ed., Routledge, Milton Park, UK **2018**, pp. 1–14.
[28] a) X. Cheng, Z. Xiang, C. Yang, Y. Li, L. Wang, Q. Zhang, *Adv. Funct. Mater.* **2024**, *34*, 2311412; b) X. Yao, Z. Khanam, C. Li, M. Koroma, T. Ouyang, Y. W. Hu, K. Shen, M. S. Balogun, *Small* **2024**, *20*, 2312036.
[29] S. Luo, J. Cui, S. Liang, Y. Guo, B. Yuan, L. Xu, R. Zheng, J. Li, W. Yang, M. Chen, Y. Lu, Y. Luo, *J. Mater. Chem. C* **2024**, *12*, 6153.
[30] Q. Liang, Q. Zhang, X. Zhao, M. Liu, A. T. Wee, *ACS Nano* **2021**, *15*, 2165.
[31] Z. Liu, H. Sun, L. Qin, X. Cao, J. Zhou, A. Pan, G. Fang, S. Liang, *ChemNanoMat* **2020**, *6*, 1553.
[32] a) H. Luo, B. Wang, C. Wang, F. Wu, F. Jin, B. Cong, Y. Ning, Y. Zhou, D. Wang, H. Liu, *Energy Storage Mater.* **2020**, *33*, 390; b) J. Ding, H. Zheng, H. Gao, Q. Liu, Z. Hu, L. Han, S. Wang, S. Wu, S. Fang, S. Chou, *Adv. Energy Mater.* **2021**, *11*, 2100973; c) Z. Li, Y. Ren, L. Mo, C. Liu, K. Hsu, Y. Ding, X. Zhang, X. Li, L. Hu, D. Ji, *ACS Nano* **2020**, *14*, 5581; d) J. Kim, S. H. Lee, C. Park, H. S. Kim, J. H. Park, K. Y. Chung, H. Ahn, *Adv. Funct. Mater.* **2021**, *31*, 2100005.
[33] M. Liao, J. Wang, L. Ye, H. Sun, Y. Wen, C. Wang, X. Sun, B. Wang, H. Peng, *Angew. Chem.* **2020**, *132*, 2293.
[34] P. He, S. Chen, *Electrochem. Sci. Adv.* **2022**, *2*, 2100090.
[35] W. Bi, G. Gao, G. Wu, M. Atif, M. AlSalhi, G. Cao, *Energy Storage Mater.* **2021**, *40*, 209.
[36] a) Y. Lin, F. Zhou, M. Xie, S. Zhang, C. Deng, *ChemSusChem* **2020**, *13*, 3696; b) J. Cao, D. Zhang, Y. Yue, X. Wang, T. Pakornchote, T. Bovornratanaraks, X. Zhang, Z.-S. Wu, J. Qin, *Nano Energy* **2021**, *84*, 105876; c) X. Liang, J. Hao, B. Tan, X. Lu, W. Li, *J. Power Sources* **2020**, *472*, 228507; d) Z. Zhang, B. Xi, X. Wang, X. Ma, W. Chen, J. Feng, S. Xiong, *Adv. Funct. Mater.* **2021**, *31*, 2103070.
[37] J. Li, N. Luo, F. Wan, S. Zhao, Z. Li, W. Li, J. Guo, P. R. Shearing, D. J. Brett, C. J. Carmalt, *Nanoscale* **2020**, *12*, 20638.
[38] a) W. Yang, L. Dong, W. Yang, C. Xu, G. Shao, G. Wang, *Small Methods* **2020**, *4*, 1900670; b) D. Bin, W. Huo, Y. Yuan, J. Huang, Y. Liu, Y. Zhang, F. Dong, Y. Wang, Y. Xia, *Chem* **2020**, *6*, 968.
[39] Y. Du, X. Wang, J. Sun, *Nano Res.* **2021**, *14*, 754.
[40] a) A. Van der Ven, J. Bhattacharya, A. A. Belak, *Acc. Chem. Res.* **2013**, *46*, 1216; b) K. Toyoura, Y. Koyama, A. Kuwabara, F. Oba, I. Tanaka, *Phys. Rev. B* **2008**, *78*, 214303.
[41] a) G. H. Vineyard, *J. Phys. Chem. Solids* **1957**, *3*, 121; b) J. Meng, H. Guo, C. Niu, Y. Zhao, L. Xu, Q. Li, L. Mai, *Joule* **2017**, *1*, 522.
[42] Q. Zong, W. Du, C. Liu, H. Yang, Q. Zhang, Z. Zhou, M. Atif, M. Alsalhi, G. Cao, *Nano-Micro Lett.* **2021**, *13*, 116.
[43] Y. Li, D. Zhang, S. Huang, H. Y. Yang, *Nano Energy* **2021**, *85*, 105969.
[44] H. Geng, M. Cheng, B. Wang, Y. Yang, Y. Zhang, C. C. Li, *Adv. Funct. Mater.* **2020**, *30*, 1907684.
[45] C. Liu, Z. Neale, J. Zheng, X. Jia, J. Huang, M. Yan, M. Tian, M. Wang, J. Yang, G. Cao, *Energy Environ. Sci.* **2019**, *12*, 2273.
[46] M. Du, C. Liu, F. Zhang, W. Dong, X. Zhang, Y. Sang, J. J. Wang, Y. G. Guo, H. Liu, S. Wang, *Adv. Sci.* **2020**, *7*, 2000083.
[47] Y. Yang, Y. Tang, S. Liang, Z. Wu, G. Fang, X. Cao, C. Wang, T. Lin, A. Pan, J. Zhou, *Nano Energy* **2019**, *61*, 617.
[48] X. Zhou, Y. Li, J. Chen, Q. Zheng, Y. Huo, F. Xie, D. Lin, *Chem. Eng. J.* **2023**, *471*, 144738.
[49] D. Kundu, B. D. Adams, V. Duffort, S. H. Vajargah, L. F. Nazar, *Nat. Energy* **2016**, *1*, 16119.
[50] Y. Yang, Y. Tang, G. Fang, L. Shan, J. Guo, W. Zhang, C. Wang, L. Wang, J. Zhou, S. Liang, *Energy Environ. Sci.* **2018**, *11*, 3157.
[51] P. He, G. Zhang, X. Liao, M. Yan, X. Xu, Q. An, J. Liu, L. Mai, *Adv. Energy Mater.* **2018**, *8*, 1702463.
[52] B. Tang, G. Fang, J. Zhou, L. Wang, Y. Lei, C. Wang, T. Lin, Y. Tang, S. Liang, *Nano Energy* **2018**, *51*, 579.
[53] H. Wang, L. Lei, Z. Li, L. Huang, T. Wei, C. Wang, X. Wei, *Energy Fuels* **2022**, *36*, 2872.
[54] X. Liu, H. Zhang, D. Geiger, J. Han, A. Varzi, U. Kaiser, A. Moretti, S. Passerini, *Chem. Commun.* **2019**, *55*, 2265.
[55] J. Li, K. McColl, X. Lu, S. Sathasivam, H. Dong, L. Kang, Z. Li, S. Zhao, A. G. Kafizas, R. Wang, *Adv. Energy Mater.* **2020**, *10*, 2000058.
[56] W. Xu, C. Sun, N. Wang, X. Liao, K. Zhao, G. Yao, Q. Sun, H. Cheng, Y. Wang, X. Lu, *Nano Energy* **2021**, *81*, 105584.
[57] T. Wei, K. Ma, G. Yang, C. Wang, *ACS Appl. Mater. Interfaces* **2019**, *11*, 20888.
[58] a) B. Tang, L. Shan, S. Liang, J. Zhou, *Energy Environ. Sci.* **2019**, *12*, 3288; b) F. Wan, L. Zhang, X. Dai, X. Wang, Z. Niu, J. Chen, *Nat. Commun.* **2018**, *9*, 1656.
[59] a) Y. Lu, T. Zhu, W. van den Bergh, M. Stefik, K. Huang, *Angew. Chem., Int. Ed.* **2020**, *59*, 17004; b) L. Zhang, B. Zhang, J. Hu, J. Liu, L. Miao, J. Jiang, *Small Methods* **2021**, *5*, 2100094.
[60] X. Wang, B. Xi, X. Ma, Z. Feng, Y. Jia, J. Feng, Y. Qian, S. Xiong, *Nano Lett.* **2020**, *20*, 2899.
[61] B. Tang, J. Zhou, G. Fang, F. Liu, C. Zhu, C. Wang, A. Pan, S. Liang, *J. Mater. Chem. A* **2019**, *7*, 940.
[62] H. Tian, Y. He, L. Wang, Y. Lai, J. Wang, H. Xiang, W. Zhao, L. Zhang, *Mater. Chem. Front.* **2022**, *6*, 1920.
[63] L. Ma, N. Li, C. Long, B. Dong, D. Fang, Z. Liu, Y. Zhao, X. Li, J. Fan, S. Chen, *Adv. Funct. Mater.* **2019**, *29*, 1906142.
[64] F. Xiong, S. Tan, X. Yao, Q. An, L. Mai, *Mater. Today* **2021**, *45*, 169.
[65] a) W. Li, K. Wang, S. Cheng, K. Jiang, *Energy Storage Mater.* **2018**, *15*, 14; b) G. Li, Z. Yang, Y. Jiang, C. Jin, W. Huang, X. Ding, Y. Huang, *Nano Energy* **2016**, *25*, 211.
[66] X. Liang, L. Yan, W. Li, Y. Bai, C. Zhu, Y. Qiang, B. Xiong, B. Xiang, X. Zou, *Nano Energy* **2021**, *87*, 106164.
[67] H. H. Kristoffersen, H. Metiu, *T. Phys. Chem. C* **2016**, *120*, 3986.
[68] a) M. Yan, P. He, Y. Chen, S. Wang, Q. Wei, K. Zhao, X. Xu, Q. An, Y. Shuang, Y. Shao, *Adv. Mater.* **2018**, *30*, 1703725; b) H. Jiang, Y. Zhang, Z. Pan, L. Xu, J. Zheng, Z. Gao, T. Hu, C. Meng, J. Wang, *Mater. Chem. Front.* **2020**, *4*, 1434.
[69] Y. Tao, D. Huang, H. Chen, Y. Luo, *ACS Appl. Mater. Interfaces* **2021**, *13*, 16576.
[70] J. Shin, D. S. Choi, H. J. Lee, Y. Jung, J. W. Choi, *Adv. Energy Mater.* **2019**, *9*, 1900083.
[71] D. Kundu, S. H. Vajargah, L. Wan, B. Adams, D. Prendergast, L. F. Nazar, *Energy Environ. Sci.* **2018**, *11*, 881.
[72] F. Wang, W. Sun, Z. Shadike, E. Hu, X. Ji, T. Gao, X. Q. Yang, K. Xu, C. Wang, *Angew. Chem.* **2018**, *130*, 12154.
[73] a) T. Wu, K. Zhu, C. Qin, K. Huang, *J. Mater. Chem. A* **2019**, *7*, 5612; b) S. Zhang, H. Tan, X. Rui, Y. Yu, *Acc. Chem. Res.* **2020**, *53*, 1660.
[74] R. Wei, X. Wang, B. Xi, Z. Feng, H. Li, W. Chen, Y. Jia, J. Feng, S. Xiong, *ACS Appl. Energy Mater.* **2020**, *3*, 5343.
[75] K. Zhu, T. Wu, K. Huang, *Adv. Energy Mater.* **2019**, *9*, 1901968.
[76] F. Ming, H. Liang, Y. Lei, S. Kandambeth, M. Eddaoudi, H. N. Alshareef, *ACS Energy Lett.* **2018**, *3*, 2602.
[77] P. Luo, W. Zhang, S. Wang, G. Liu, Y. Xiao, C. Zuo, W. Tang, X. Fu, S. Dong, *J. Alloys Compd.* **2021**, *884*, 161147.
[78] Z. Wei, D. Wang, X. Yang, C. Wang, G. Chen, F. Du, *Adv. Mater. Interfaces* **2018**, *5*, 1800639.
[79] M. Du, Z. Miao, H. Li, Y. Sang, H. Liu, S. Wang, *J. Mater. Chem. A* **2021**, *9*, 19245.
[80] Y. Luo, L. Wei, H. Geng, Y. Zhang, Y. Yang, C. C. Li, *ACS Appl. Mater. Interfaces* **2020**, *12*, 11753.
[81] X. Wang, Y. Li, P. Das, S. Zheng, F. Zhou, Z.-S. Wu, *Energy Storage Mater.* **2020**, *31*, 156.
[82] B. Ju, H. J. Song, H. Yoon, D.-W. Kim, *Chem. Eng. J.* **2021**, *420*, 130528.

© 2024 The Author(s). Advanced Energy Materials published by Wiley-VCH GmbH

16146840, 2024, 31, Downloaded from https://advanced.onlinelibrary.wiley.com/doi/10.1002/aenm.202401704 by University of Adelaide Alumni, Wiley Online Library on [02/04/2025]. See the Terms and Conditions (https://onlinelibrary.wiley.com/terms-and-conditions) on Wiley Online Library for rules of use; OA articles are governed by the applicable Creative Commons License

[83] a) E. Uchaker, Y. Zheng, S. Li, S. Candelaria, S. Hu, G. Cao, *J. Mater. Chem. A* **2014**, *2*, 18208; b) X. Jia, C. Liu, Z. G. Neale, J. Yang, G. Cao, *Chem. Rev.* **2020**, *120*, 7795.
[84] X. Wang, Y. Li, S. Wang, F. Zhou, P. Das, C. Sun, S. Zheng, Z. S. Wu, *Adv. Energy Mater.* **2020**, *10*, 2000081.
[85] S. Deng, Z. Yuan, Z. Tie, C. Wang, L. Song, Z. Niu, *Angew. Chem., Int. Ed.* **2020**, *59*, 22002.
[86] Y. Liu, Y. Zhang, H. Jiang, J. Sun, Z. Feng, T. Hu, C. Meng, Z. Pan, *Chem. Eng. J.* **2022**, *435*, 134949.
[87] W. Zhang, Y. Xiao, C. Zuo, W. Tang, G. Liu, S. Wang, W. Cai, S. Dong, P. Luo, *ChemSusChem* **2021**, *14*, 971.
[88] Z. Qi, T. Xiong, T. Chen, W. Shi, M. Zhang, Z. W. J. Ang, H. Fan, H. Xiao, W. S. V. Lee, J. Xue, *J. Alloys Compd.* **2021**, *870*, 159403.
[89] Y. Bai, H. Zhang, B. Xiang, J. Hao, L. Yan, C. Zhu, *Chem. Eng. J.* **2021**, *420*, 130474.
[90] Y. G. Lee, G. Yoo, Y. R. Jo, H. R. An, B. R. Koo, G. H. An, *Adv. Energy Mater.* **2023**, *13*, 2300630.
[91] P. Zhang, Y. Gong, S. Fan, Z. Luo, J. Hu, C. Peng, Q. Zhang, Y. Li, X. Ren, *Adv. Energy Mater.* **2024**, 2401493.
[92] F. Liang, M. Chen, S. Zhang, Z. Zou, C. Ge, S. Jia, S. Le, F. Yu, J. Nong, *ACS Sustainable Chem. Eng.* **2024**, *12*, 5117.
[93] S. Li, X. Xu, W. Chen, J. Zhao, K. Wang, J. Shen, X. Chen, X. Lu, X. Jiao, Y. Liu, *Energy Storage Mater.* **2024**, *65*, 103108.
[94] F. Wu, Y. Wang, X. Dai, S. Meng, D. Zheng, R. Yin, W. Liu, W. Shi, X. Cao, *ACS Appl. Energy Mater.* **2023**, *6*, 2680.
[95] B.-S. Yin, S.-W. Zhang, T. Xiong, W. Shi, K. Ke, W. S. V. Lee, J. Xue, Z.-B. Wang, *New J. Chem.* **2020**, *44*, 15951.
[96] Q. Zong, Y. Zhuang, C. Liu, Q. Kang, Y. Wu, J. Zhang, J. Wang, D. Tao, Q. Zhang, G. Cao, *Adv. Energy Mater.* **2023**, *13*, 2301480.
[97] J. Zhang, R. Liu, C. Huang, C. Dong, L. Xu, L. Yuan, S. Lu, L. Wang, L. Zhang, L. Chen, *Nano Energy* **2024**, *122*, 109301.
[98] R. Liu, J. Zhang, C. Huang, C. Dong, L. Xu, B. Zhu, L. Wang, L. Zhang, L. Chen, *J. Colloid Interface Sci.* **2024**, *654*, 279.
[99] Y. Liu, J. Zhang, Y. Liu, M. Zhang, Z. Pan, K. Cai, *Small* **2024**, *20*, 2401922.
[100] L. Shan, Y. Yang, W. Zhang, H. Chen, G. Fang, J. Zhou, S. Liang, *Energy Storage Mater.* **2019**, *18*, 10.
[101] Q. Pang, W. He, X. Yu, S. Yang, H. Zhao, Y. Fu, M. Xing, Y. Tian, X. Luo, Y. Wei, *Appl. Surf. Sci.* **2021**, *538*, 148043.
[102] G. Su, S. Chen, H. Dong, Y. Cheng, Q. Liu, H. Wei, E. H. Ang, H. Geng, C. C. Li, *Nanoscale* **2021**, *13*, 2399.
[103] Z. Chen, H. Liu, S. Fan, Q. Zhang, C. Yuan, W. Peng, Y. Li, X. Fan, *Adv. Energy Mater.* **2024**, *14*, 2400977.
[104] Y. Zhang, F. Wan, S. Huang, S. Wang, Z. Niu, J. Chen, *Nat. Commun.* **2020**, *11*, 2199.
[105] L. Wang, K.-W. Huang, J. Chen, J. Zheng, *Sci. Adv.* **2019**, *5*, aax4279.
[106] F. Li, H. Sheng, H. Ma, Y. Qi, M. Shao, J. Yuan, W. Li, W. Lan, *ACS Appl. Energy Mater.* **2023**, *6*, 6201.
[107] J. Zheng, C. Liu, M. Tian, X. Jia, E. P. Jahrman, G. T. Seidler, S. Zhang, Y. Liu, Y. Zhang, C. Meng, *Nano Energy* **2020**, *70*, 104519.
[108] C. Xia, J. Guo, P. Li, X. Zhang, H. N. Alshareef, *Angew. Chem., Int. Ed.* **2018**, *57*, 3943.
[109] S. Islam, M. H. Alfaruqi, D. Y. Putro, V. Soundharrajan, B. Sambandam, J. Jo, S. Park, S. Lee, V. Mathew, J. Kim, *J. Mater. Chem. A* **2019**, *7*, 20335.
[110] S. Zhang, Z. Zou, Y. Gao, J. Geng, M. Chen, W. Ling, F. Liang, X. Peng, M. Zhou, F. Yu, *Nano Energy* **2023**, *115*, 108736.
[111] Q. Sun, H. Cheng, Y. Yuan, Y. Liu, W. Nie, K. Zhao, K. Wang, W. Yao, X. Lu, J. Lu, *Adv. Energy Mater.* **2023**, *13*, 2202515.
[112] J. Zeng, Z. Zhang, X. Guo, G. Li, *J. Mater. Chem. A* **2019**, *7*, 21079.
[113] R. Pan, F. Cui, A. Zheng, G. Zhang, Z. Jiang, Y. Xiong, L. Wei, Q. Zhang, L. Sun, K. Yin, *Adv. Funct. Mater.* **2023**, *33*, 2300619.
[114] Y. Ma, W. Cao, Y. Liu, Q. Li, S. Cai, S. j. Bao, M. Xu, *Small* **2024**, *20*, 2306790.
[115] T.-T. Fang, in *Elements of Structures and Defects of Crystalline Materials*, (Ed.: T.-T. Fang), Elsevier, **2018**, pp. 169–197.
[116] D. Wu, Z. Wen, H. Jiang, H. Li, Y. Zhuang, J. Li, Y. Yang, J. Zeng, J. Cheng, J. Zhao, *ACS Appl. Mater. Interfaces* **2021**, *13*, 12049.
[117] Y. Lin, F. Zhou, M. Chen, S. Zhang, C. Deng, *Chem. Eng. J.* **2020**, *396*, 125259.
[118] L. Kong, M. Shao, Q. Xie, J. Liu, Y. Qian, *J. Cryst. Growth* **2004**, *260*, 435.
[119] J. Wan, X. Yao, X. Gao, X. Xiao, T. Li, J. Wu, W. Sun, Z. Hu, H. Yu, L. Huang, *Adv. Funct. Mater.* **2016**, *26*, 7263.
[120] Z. Su, J. Liu, M. Li, Y. Zhu, S. Qian, M. Weng, J. Zheng, Y. Zhong, F. Pan, S. Zhang, *Electrochem. Energy Rev.* **2020**, *3*, 286.
[121] Q. Wang, Y. Lei, D. Wang, Y. Li, *Energy Environ. Sci.* **2019**, *12*, 1730.
[122] P. Byeon, Y. Hong, H. B. Bae, J. Shin, J. W. Choi, S.-Y. Chung, *Nat. Commun.* **2021**, *12*, 4599.
[123] T. He, Y. Ye, H. Li, S. Weng, Q. Zhang, M. Li, T. Liu, J. Cheng, X. Wang, J. Lu, *Mater. Today* **2021**, *43*, 53.
[124] Z. Xiao, C. Xie, Y. Wang, R. Chen, S. Wang, *J. Energy Chem.* **2021**, *53*, 208.
[125] S. Gao, B. Gu, X. Jiao, Y. Sun, X. Zu, F. Yang, W. Zhu, C. Wang, Z. Feng, B. Ye, *J. Am. Chem. Soc.* **2017**, *139*, 3438.
[126] Y. Bai, H. Zhang, B. Xiang, X. Liang, J. Hao, C. Zhu, L. Yan, *ACS Appl. Mater. Interfaces* **2021**, *13*, 23230.
[127] Z. Wang, P. Liang, R. Zhang, Z. Liu, W. Li, Z. Pan, H. Yang, X. Shen, J. Wang, *Appl. Surf. Sci.* **2021**, *562*, 150196.
[128] H. Zhang, J. Wang, Q. Liu, W. He, Z. Lai, X. Zhang, M. Yu, Y. Tong, X. Lu, *Energy Storage Mater.* **2019**, *21*, 154.
[129] S. Sultana, S. Mansingh, K. Parida, *Mater. Adv.* **2021**, *2*, 6942.



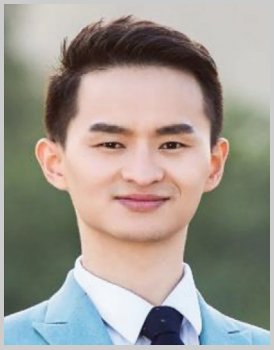
Xin Zeng received her M.Phil. degree from the University of Sydney in 2019. She is currently pursuing her Ph.D. at the School of Chemical and Biomolecular Engineering, the University of Sydney, Australia. Her research focuses on zinc-based flexible energy storage devices.

© 2024 The Author(s). Advanced Energy Materials published by Wiley-VCH GmbH

16146840, 2024, 31, Downloaded from https://advanced.onlinelibrary.wiley.com/doi/10.1002/aenm.202401704 by University of Adelaide Alumni, Wiley Online Library on [02/04/2025]. See the Terms and Conditions (https://onlinelibrary.wiley.com/terms-and-conditions) on Wiley Online Library for rules of use; OA articles are governed by the applicable Creative Commons License



Cheng Wang obtained his B.Sc. from Beijing University of Chemical Technology. He subsequently earned his M.Sc. in 2019 and his Ph.D. in 2023, both from the University of Sydney. He is currently a research fellow at the University of Adelaide, Australia. His current research centers on electrochemistry, with a particular focus on the development of electrolytes and inorganic battery materials for aqueous zinc-ion batteries.



Zengxia Pei received his Ph.D. from City University of Hong Kong. He is currently a lecturer and horizon fellow at the University of Sydney. His works focus on nanomaterials for sustainable energy storage and conversion, with special interests in aqueous batteries, polymer electrolytes, and electrocatalysis. He was consecutively recognized as a Global Highly Cited Researcher (Top 1%) in 2020-2023, and was named the Australian Research Top Rising Star (1 out of 5 in Chemical/Material Science) from 2019 to 2021.

© 2024 The Author(s). Advanced Energy Materials published by Wiley-VCH GmbH

16146840, 2024, 31, Downloaded from https://advanced.onlinelibrary.wiley.com/doi/10.1002/aenm.202401704 by University of Adelaide Alumni, Wiley Online Library on [02/04/2025]. See the Terms and Conditions (https://onlinelibrary.wiley.com/terms-and-conditions) on Wiley Online Library for rules of use; OA articles are governed by the applicable Creative Commons License